

Rigid flocks, undulatory gaits, and chiral foldamers from chemical self-interaction in a freely-jointed active colloidal chain

Arvin Gopal Subramaniam,^{1,2,*} Manoj Kumar,³ Shashi Thutupalli,^{3,4} and Rajesh Singh^{1,2,†}

¹*Department of Physics, Indian Institute of Technology Madras, Chennai, India*

²*Center for Soft and Biological Matter, IIT Madras, Chennai, India*

³*Simons Centre for the Study of Living Machines, National Centre for Biological Sciences, Tata Institute of Fundamental Research, Bangalore, India*

⁴*International Centre for Theoretical Sciences, Tata Institute of Fundamental Research, Bangalore, India*

Active matter systems - such as a collection of active colloidal particles - operate far from equilibrium with complex inter-particle interactions that govern their collective dynamics. Predicting the collective dynamics of such systems may aid the design of self-shaping structures comprised of active colloidal units with a prescribed dynamical function. Here, using simulations and theory, we study the collective dynamics of a chain consisting of active Brownian particles with internal interactions via trail-mediated chemicals, connected by harmonic springs in two dimensions to obtain design principles for active colloidal molecules. We show that two-dimensional confinement and chemo-repulsive interactions between the freely-jointed particles lead to an emergent rigidity of the chain in the steady-state dynamics. In the chemo-attractive regime, the chain collapses into crystals that abruptly halt their motion. Further, in a chain consisting of a binary mixture of monomers, we show that non-reciprocal chemical affinities between distinct species give rise to novel phenomena, such as chiral molecules with tunable dynamics, sustained undulatory gaits and reversal of the direction of motion. Our results suggest a novel interpretation of the role of trail-mediated interactions, in addition to providing active self-assembly principles.

I. INTRODUCTION

Active colloidal particles are a class of active matter that exhibit rich collective phenomenon at the many-body dynamical level [1, 2]. Such systems include those of biological [3] or synthetic [4] origin, with propulsion mechanisms being due to locally generated surface processes [4, 5] or externally applied fields [5–7]. The dynamics of extended bodies of these active colloids is a wide area of current research [6–11], with various self-organized dynamical topologies reported - including linear [8, 12], C-shaped [8], helical [7, 8, 13], rings [10], and rotating chiral clusters [9].

Another parallel long-standing goal of soft matter science is the self-assembly rules of colloidal particles into targeted self-shaping structures [2, 14]. In these works, the object of interest typically is the *structural* details (for instance the configuration) of the self-assembled colloidal molecule [15]. Out-of-equilibrium system, the emergent dynamics exhibited by the system is of interest, and the ability to design extended collective with a prescribed dynamical function [16, 17] is instead of interest.

A specific class of colloidal interactions are those that are mediated by a chemical trail [18–20]. These interactions have also been widely reported in various biological systems - including bacteria [21] and ant colonies [22], with demonstrated roles in biofilm [23] and colony [24] formation. Theoretically, these have been studied at

the individual [25, 26], and collective [19, 23] levels. Recently, it has been demonstrated (experimentally) that the trail mediated chemo-repulsive interactions between the monomers of an active colloidal chain results in an emergent C-shape rigidity of the chain [27].

In this paper, we study the trail-mediated collective dynamics of a collection of chemically self-interacting active colloids joint by harmonic springs - which we term an *active colloidal chain*. We cover the full range of chemo-repulsive, chemo-attractive, and non-reciprocal chemical interactions between the monomers of the chain. A summary of the interaction types studied here is shown in Fig. (1). Our model, consisting of two basic ingredients - trail-mediated chemotactic interactions between monomers and internal spring forces - we show to be able to support a wide range of phenomenology. In monodisperse chains, we report “universal” C-shape flocks in the chemo-repulsive case, with the universality arising via the forward-backward symmetry breaking due to the presence of chemical trails, and crystallization in the chemo-attractive case. In a bidisperse chain (made of two species of monomers shown in Fig. (1)), we show that undulatory gaits of purely chemical origin are supported, in addition to chiral molecules with tunable dynamics. Our model thus uncovers a role of trail-mediated interactions in sustaining a spatio-temporal asymmetry in colloidal dynamics, whilst providing a simple yet scalable model of tunable non-equilibrium self-assembly of active colloids.

This paper is organized as follows. In Section II, we introduce our model of a chemically interacting chain of active colloidal particles, and specify important length and time scales, as well as dimensionless parameters that arise. In Sections III and IV of the paper, we study the dynamics of the system via relevant length and

* ph22d800@smail.iitm.ac.in

† rsingh@physics.iitm.ac.in

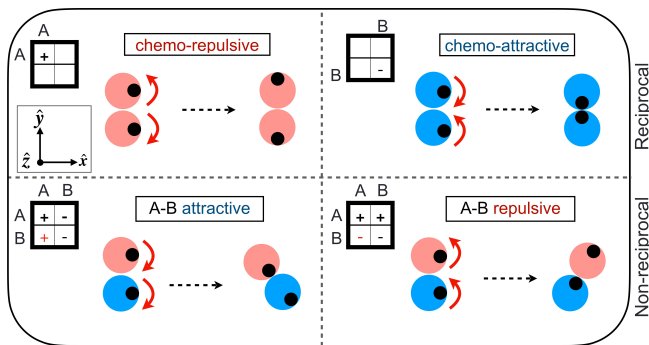


FIG. 1. Schematic diagram for chemical interaction of a dimer. Two species of A type (red color) are purely repulsive, while those of B type (blue color) are purely attractive. The monomers are free to rotate and slide on each other, while the distance between the monomers does not change because they are freely-jointed. For repulsive interactions, monomers preferentially point away from each other, whilst for attractive interactions they preferentially point towards each other. For a dimer of both A and B types, the interactions are non-reciprocal (*bottom row*). There are two choices: A attracts B and B is repelled away from A and vice-versa. The black dot indicate the orientation of the particles, while curved red arrows show rotations. Interaction matrices in the inset imply attraction (-) or repulsion (+) between monomers. These matrices specify the nature of both self-interaction as well as inter-particle interactions. The full interaction matrices are represented by Υ in Eq.(5).

time scales that govern the overall qualitative behaviour; along with time-averaged order parameters that provide quantitative-predictions. We obtain a full phase diagram of chemo-repulsive and attractive cases, with different regions delimited by different relative contributions of these length and time scales. Then, in Sections V, we study a chain made of two species of monomers with non-reciprocal chemical affinities. In these chains, we report the existence of novel emergent dynamics - sustained oscillations, reversal of motion, and undulatory propulsion (a swimming gait). In section VI, we show how specifically chosen initial configurations and/or conditions can lead to a chirality in the dynamics. We conclude by suggesting how such assemblies can be used to achieve a programmable dynamics, where the structural and dynamical details of the colloidal molecule can be engineered by tuning the interaction details between species in the chain and/or the initial conditions. Finally, we discuss implications of our work and potential future studies.

II. MODEL

A. Equations of motion

We model the i th active particle as a colloid particle centered at $\mathbf{r}_i = (x_i, y_i)$, confined to move in two-dimensions, which self-propels with a speed v_s , along the

directions $\mathbf{e}_i = (\cos \theta_i, \sin \theta_i)$. Here $i = 1, 2, 3, \dots, N$. The direction of the i th particle, given by the angle θ_i , changes due to coupling its dynamics to the dynamics of a phoretic (scalar) field c , which we describe below. The position and orientation of the i th particle is updated as:

$$\frac{d\mathbf{r}_i}{dt} = \mathbf{V}_i, \quad \frac{d\mathbf{e}_i}{dt} = \boldsymbol{\Omega}_i \times \mathbf{e}_i. \quad (1)$$

Here, the translational velocity \mathbf{V}_i and angular velocity $\boldsymbol{\Omega}_i$ of the i th particle are given as:

$$\mathbf{V}_i = v_s \mathbf{e}_i + \chi_t \mathbf{J}_i + \mu \mathbf{F}_i + \sqrt{2D_t} \boldsymbol{\xi}_i^T, \quad (2a)$$

$$\boldsymbol{\Omega}_i = \chi_r (\mathbf{e}_i \times \mathbf{J}_i) + \sqrt{2D_r} \boldsymbol{\xi}_i^R. \quad (2b)$$

In the above, μ is mobility, D_t and D_r , are respectively, translational and rotational diffusion constants of the particle, while $\boldsymbol{\xi}_i^T$ and $\boldsymbol{\xi}_i^R$ are white noises. The chemical interaction between the particles is given in terms of the chemical current \mathbf{J}_i , which is described in detail below. The chemical interactions in our model (2) drive orientational changes through the terms proportional to χ_r . The case of $\chi_r < 0$ (the *chemo-attractive* case) corresponding to monomers rotating towards each other, while $\chi_r > 0$ (the *chemo-repulsive* case) implies that the particles rotate away from each other. This scenario corresponds to the well known mechanism of repulsion due to the trails of other monomers in the system [20, 27, 28]. Similarly, the term proportional to χ_t ensures repulsion or attraction in the positional dynamics.

The force keeping the chain together is modelled as a spring. The body force on the i th particle is given as: $\mathbf{F}_i = -\nabla_i \mathcal{U}$, while the potential \mathcal{U} is: $\mathcal{U} = \sum_{i=1}^{N-1} \mathcal{U}^s(\mathbf{r}_i, \mathbf{r}_{i+1}) + \sum_{i < j} \mathcal{U}^e(\mathbf{r}_i, \mathbf{r}_j)$. Here, $\mathcal{U}^s = k_{sp} (r_{ij} - 2b)^2$ is spring potential of stiffness k_{sp} and natural length $2b$ which holds the chain together and only acts between neighbouring particles in the chain. $r_{ij} = |\mathbf{r}_i - \mathbf{r}_j|$ and b is the radius of the monomers. \mathcal{U}^e is a repulsive potential precluding overlap of particles. We choose it to be also of the form $\mathcal{U}^e = k^e (r_{ij} - 2b)^2$ if $r_{ij} < 2b$, while it vanishes otherwise. k^e is a constant, which determines the strength of the repulsive force, which precludes overlap of particles. Note that there is no bending potential added. Thus, we expect the chain to be highly flexible. We show below (section III) that chemical interaction between the monomers of the chain leads to an emergent rigidity in the chain.

The chemical interaction between the particles is given in terms of chemical current \mathbf{J}_i (see Eq. (2)), which is defined as:

$$\mathbf{J}_i(t) = -[\nabla c(\mathbf{r}, t)]_{\mathbf{r}=\mathbf{r}_i} \quad (3)$$

where $c(\mathbf{r}, t)$ is the concentration of filled micelles at the location \mathbf{r} at time t . In our model, where each particle is considered as a point source of chemicals, the dynamics of the field c follows from the equation:

$$\frac{\partial c(\mathbf{r}, t)}{\partial t} = D_c \nabla^2 c(\mathbf{r}, t) + \sum_{i=1}^N c_0 \delta(\mathbf{r} - \mathbf{r}_i). \quad (4)$$

Here D_c is the diffusion coefficient of the filled micelles, c_0 is emission constant of the micelles, and N is the number of monomers in the chain. It should be noted that we model the particle as a point emitter of chemicals. Using the above, we can solve for $\mathbf{J}_i(t)$ as:

$$\mathbf{J}_i(t) = \frac{c_0}{\pi b} \sum_{j=1}^N \left[\Upsilon_{ij} \int_0^{t-t_0} dt' \frac{\mathbf{r}_i(t) - \mathbf{r}_j(t')}{\mathcal{D}^2} \mathcal{F}_{ij}(t, t') \right]. \quad (5)$$

Here $\mathcal{F}_{ij}(t, t') = \exp(-[\mathbf{r}_i(t) - \mathbf{r}_j(t')]^2/\mathcal{D})$ and $\mathcal{D} = 4D_c|t - t'|$, while t_0 is a finite time delay between the chemical being released and sensed, which preempts any divergence in the mathematical form of $\mathbf{J}_i(t)$ [18]. In simulations, we choose t_0 to be much smaller than any other time-scale in the problem. The tensor Υ contains our choice of chemical affinities. We explain our choice of non-reciprocal affinities in Section (V) below. A pictorial representation of Υ for dimers is in the inset matrices of Fig. 1. The above model was previously used in a recent work [27] to capture experimental phenomenology in a Hele-Shaw cell with monomers having chemo-repulsive interactions. In this work, we study monomers with both chemo-attractive and chemo-repulsive interactions. We also allow for monomers of different kinds in the same chain, and thus, study non-reciprocal chemical self-interactions in an active chain (see Figure 1).

B. Length and time scales

We will now define some length scales and time scales that arise from this model. The basic length scale here is the monomer radius, b . This amounts to an additional length scale (imposed via excluded volume repulsion) that does not appear in Eq. (1) and (2). This is contrasted with “natural” length scales, that arise from non-dimensionalizing the equations of motion. There are three natural length scales:

$$l_c = \frac{D_c}{v_s}, \quad l_r = \frac{\chi_r}{b^2 D_r}, \quad l_t = \frac{\chi_t}{D_t}. \quad (6)$$

l_c gives the characteristic distance at which the chemical (i.e filled micelles) diffuses across the system, whilst l_r gives the characteristic amount by which monomers change their orientation in response to the chemical gradients (as opposed to spontaneously, which is simply b). l_t is the typical distance colloids translate deterministically in response to chemical gradients. There are four time scales [29], they are:

$$\tau = \frac{b}{v_s}, \quad \tau_r = \frac{1}{D_r}, \quad \tau_f = \frac{b^3}{\chi_r}, \quad \tau_c = \frac{b^2}{D_c}. \quad (7)$$

Here, τ is a spontaneous propulsion time scale, which is the time it takes for an isolated particle to move a distance equalling its radius in absence of any reorientation, τ_r is the time at which orientations turn randomly due to

noise, τ_f is a deterministic time during which the orientations change in response to the chemical field, τ_c is the time scale at which chemicals diffuse across the system.

C. Dimensionless parameters

Let us define two dimensionless activity parameters which we will use for the study:

$$\mathcal{A}_1 = \frac{bv_s}{D_c} = \frac{b}{l_d} = \frac{\tau_c}{\tau}, \quad \mathcal{A}_2 = \frac{\chi_r}{b^3 D_r} = \frac{l_r}{b} = \frac{\tau_r}{\tau_f}. \quad (8)$$

Here we have used equations (6) and (7). \mathcal{A}_1 captures the relative effect of spontaneous propulsion versus diffusion of filled micelles in the system, which in turn induces the *deterministic* rotation. Intuitively, for a sufficiently large \mathcal{A}_1 the monomers evade the diffusing chemicals and no chemically-induced self-organization will be possible, whereas below a threshold, the chemicals are sufficient diffused such that the chemical contribution is evident. We will later see in Sections III and IV that this intuition is reproduced in the simulations. \mathcal{A}_2 on the other hand captures the relative contribution of deterministic versus random rotations of the orientations. The relative contributions of these various length and time scales, where appropriate, will be discussed in the context of the qualitative behaviour of the chain, in Sections III when discussing the phase diagram [30].

III. AN ACTIVE CHAIN OF CHEMO-REPULSIVE MONOMERS

We first study a chain made of only one kind of monomers, which are chemo-repulsive in nature. The Υ matrix here has the form $\Upsilon_{ij} = 1 \quad \forall i, j$. We study the phase behaviour of the system as a function of \mathcal{A}_1 and \mathcal{A}_2 . We note that, throughout the paper, we vary \mathcal{A}_1 by varying D_c at a fixed v_s , whilst we vary \mathcal{A}_2 by varying D_r at a fixed χ_r . Our results for a chain made of chemo-repulsive monomers are summarized in the phase diagram of Fig. (2), delimited by the curvature of the steady state chain. We quantify the curvature of the chain via the Monge representation [31]. In particular, we compute $\kappa = \left\langle \nabla \cdot \left[\nabla h_i / \sqrt{1 + |\nabla h_i|^2} \right] \right\rangle$ where h_i is the height function of the chain, evaluated at each monomer location, measured from the vertical line connecting the edge monomers. The average is performed across the monomers in the chain, giving a scalar value. In our case, the inner bracket is simply reduced to $\partial_y \left[\partial_y x_i(y) / \sqrt{1 + |\partial_y x_i|^2} \right]$.

A. Results : Phase diagram

We now describe the phases displayed in phase diagram of Fig. (2). Region I+ corresponds to a stiff-

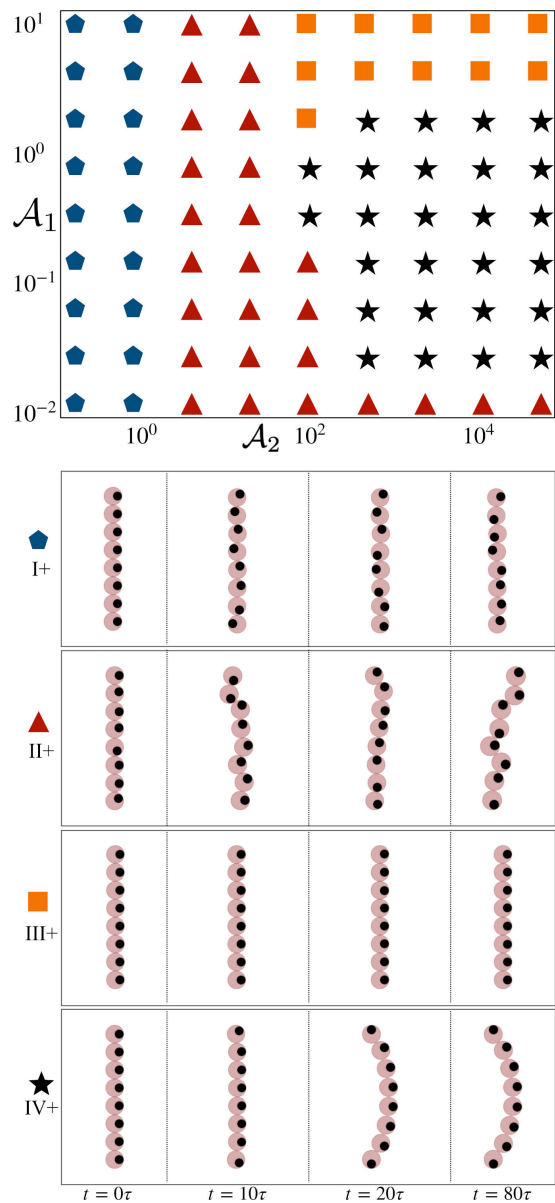


FIG. 2. Phase diagram for the chemo-repulsive case. The top panel shows the phase diagram in the \mathcal{A}_1 - \mathcal{A}_2 plane. The remaining panels show representative configuration from each distinct phase: (i) I+: Stiff + stationary chain, (ii) II+: Floppy chain (FJC-like dynamics), (iii) III+: Stiff+propelling state, (iv) rigid chain, self-propelling with C-shape. Parameters used for $(\mathcal{A}_1, \mathcal{A}_2)$ are (i) $(10^{-1}, 10^{-1})$, (ii) $(10^{-1}, 10^1)$, (iii) $(10^1, 10^3)$, (iv) $(10^{-1}, 10^4)$. Phase diagram is constructed for $N = 8$.

noisy chain (see Fig. (2)) blue symbol, also bottom panel *top row*). This is defined by a rapid τ_r with respect to τ_f , where $\frac{\tau_r}{\tau_f} = \mathcal{A}_2 \ll 1$. In this region, we also have that $\frac{l_r}{b} = \mathcal{A}_2 \ll 1$ (thus distances where the chain could potentially fold are negligible compared to the monomer radius). Note also that in this region $\tau_r/\tau_f \sim \mathcal{O}(10^{-3} - 10^{-1}) \ll \tau/\tau_f \sim \mathcal{O}(1)$, thus the chain orientations fluctuate much quicker than they can

pick up a direction of motion. Increasing \mathcal{A}_2 , we arrive at Region II+, which corresponds to a quasi-FJC (freely jointed chain) region, shown in Fig. (2), red symbol. Here, the chain translationally diffuses, but folds into and out of a given configuration (see Fig. (2) bottom panel *second to top row*). In this region we have that $\mathcal{A}_2 \sim \mathcal{O}(10^0 - 10^2)$, i.e. the diffusive (τ_r) and deterministic (τ_f) impart equal contributions of deterministic and diffusive rotational motion - resulting in the motion qualitatively resembling a freely-jointed chain - in that it neither translates nor folds deterministically [32]. Region III+ is denoted in Fig. (2) with the yellow squares. This is the weakly interacting region, where the chain propels deterministically, but does not fold (see Fig. (2), bottom panel *second to bottom row*). Here, we have that $\frac{\tau_r}{\tau_f} = \mathcal{A}_1^{-1} \ll 1$, thus the chemical diffuses much slower than the spontaneous propulsion time, and equally $\frac{l_d}{b} = \mathcal{A}_1^{-1} \ll 1$. Finally, region IV+, denoted with black symbols in Fig. (2), is the C-shape region, where the polymer propels deterministically and self-organizes into a stable configuration that resembles the alphabet C (thus acquiring a finite curvature), with a continuously varying orientation across the chain and an overall rigidity [8, 27] (see Fig. (2), bottom panel *bottom row*). We have that $\frac{\tau_r}{\tau_f} \gg 1$ (diffusive rotational time is negligible), $\tau_r \sim \tau$ (both deterministic rotation and propulsion occur simultaneously), and $\frac{l_d}{b} \gg 1$.

The characteristic dynamics of each region is shown in Fig. (2) (*bottom panel*) (Videos are in SI Video 1 [33]). After $t = 10\tau$, we see that the orientational changes in the chain have set in. The dominant time scales here are τ_r for noise-dominated phases I+ and II+, whereas for phase IV+ τ_f is dominant, with deterministic alignments seen. After $t \sim 20\tau$, we see that in phase IV+ steady-state spatial structures have formed, namely an acquisition of curvature to form a C-shape, which is identical at $t = 80\tau$.

B. Phase IV+ : Results

1. MSD, MSAD, and the curvature (κ)

We now study the phase IV+, specifically the noiseless case. In the stable C-shaped phase, dynamics can be further characterized by MSD (mean-squared displacement) and MSAD (mean-squared angular displacements), which are defined as:

$$\text{MSD}(t) = \langle [\mathbf{r}_i(t) - \mathbf{r}_i(0)]^2 \rangle, \quad (9a)$$

$$\text{MSAD}(t) = \langle [\theta_i(t) - \theta_i(0)]^2 \rangle. \quad (9b)$$

Here $\langle \dots \rangle$ denotes averaging over the monomers. We see in Fig. (3a) that the chain propels ballistically, $\text{MSD} \propto t^2$ for all values of $N \geq 3$. We note that for $N = 2$ the chain stops, this will be explained in the Section V below. The positional stiffness of the chain is quantified by curvature κ in Fig. 3(b) and (c). κ saturates as a function of time to

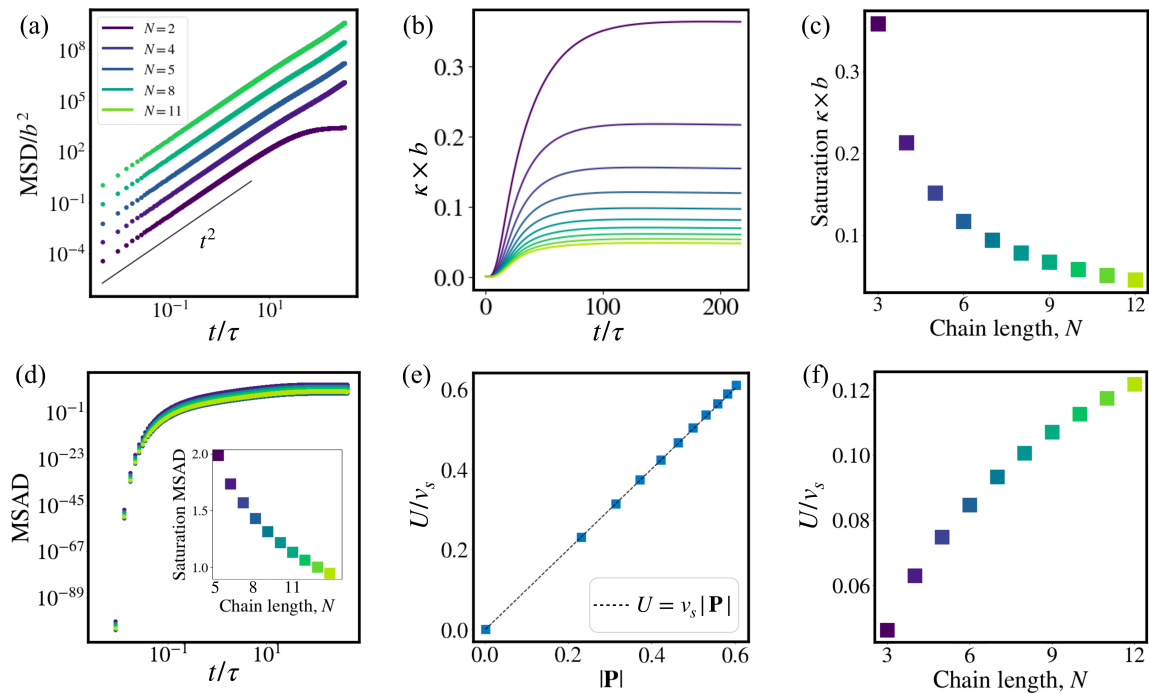


FIG. 3. Results for chemo-repulsive - Phase IV+. In panel (a), the ballistic nature of the polymers are captured via the MSD ($N = 2, 4, 5, 8,$ and 11 shown), for all except the dimer where the motion stops (see section V A). Note that the lines are vertically adjusted such that there is spacing in between for distinguishability. In (b), time evolution of the curvature is shown, which saturates to a N -dependent value in the steady-state. The saturation value of curvature (κ) of the chains as a function of N is shown in panel (c). It can be seen that longer chains are stiffer. Note that colors in (b) match to that in (c). In (d), the MSAD of the chains are shown. In the inset the saturation value is displayed, indicating now an “angular stiffening” of the chain with N . In panel (e) relation (12) is verified, whilst in (f) its value with N is shown. Thus, longer chains, which are stiffer also converge to a higher steady-state propulsion speed. Note that color bars across all panels are identical.

a N -dependent value in the steady-state. In panel (c), we plot saturation value of κ as a function of N . We see that for longer chains κ decreases and eventually saturates to a finite value, indicating “stiffer” longer chains. In panel (b), we see that the initially stiff chain acquires a curvature throughout the dynamics, saturating at a particular value after $\sim 10^2 s$. Further, the angular stiffness is quantified by the MSAD in Fig. 11(d), which also saturates. The saturation MSAD (*inset*) shows a similar decrease w.r.t N , indicating that longer chains are more “angularly stiff” in that they deviate less from $\theta_i(0)$ throughout the dynamics.

2. Speed of the chain in the steady-state

Next, we study the speed of the chain in the stable C-shape configuration. The speed of the chain can be studied by considering motion in the center of the mass (CM) frame of the references. We define the centre of the mass coordinate \mathbf{R} as:

$$\mathbf{R} = \frac{1}{N} \sum_{i=1}^N \mathbf{r}_i. \quad (10)$$

It is useful to decompose the dynamics into mutually perpendicular components. Thus, we can define velocity components parallel to the chain alignment as: $\dot{r}_i^{\parallel} = \dot{\mathbf{r}}_i \cdot \mathbf{P}$. We also define the average speed of the chain in this case as:

$$U = \langle \dot{R}^{\parallel} \rangle_{ss}, \quad \dot{R}^{\parallel} = \frac{1}{N} \sum_{i=1}^N \dot{r}_i^{\parallel} \quad (11)$$

Here $\langle \dots \rangle_{ss}$ implies that the average is taken in the steady-state. It is possible to reduce the $3N$ degrees of freedom given by equations (1), (2) to re-cast the problem in terms of the time average in Eq. (11) and Eq. (13); this dimensionality reduction procedure is explained in Appendix B. The result of this procedure yields the following equation

$$U = v_s |\mathbf{P}| \quad (12)$$

which is thus a linear relationship between *time-averaged quantity* U and an order parameter \mathbf{P} of this $3N$ dimensional system. The order parameter \mathbf{P} is net *polarisation* of the orientation of the monomers in the chain. We define the *polarization* vector \mathbf{P} as:

$$\mathbf{P} = \frac{1}{N} \sum_{i=1}^N \mathbf{e}_i. \quad (13)$$

Thus, although a linear relation akin to (12) is applicable at all times (using the instantaneous velocity instead of the time-average), the above is a unique specific case, relating a time-averaged dynamical quantity to an order parameter of the system. This is possible due to the symmetry of the dynamics as detailed in Appendix B.

A plot of U/v_s versus $|\mathbf{P}|$ is given in Fig. 11(e). Here, the simulation data is predicted by Eq. (12), validating our dimensionality reduction procedure. In Fig. 11(f), we see that the U/v_s increases with N , corresponding to the behaviour of \mathbf{P} in this limit.

3. Universality of the C-shape

The bottom panel of Fig. (2) contains the phase IV+. It shows that in the steady-state, the chain acquires a stable C-shape. This C-shape is indeed acquired for any initial conditions (see SI Video 3 [33]), and thus the solution is said to be *universal*. This result is a consequence of the *history dependence* (a.k.a trail-mediation) of the dynamics (c.f. Eq. (5)), in that the colloids preferentially point away from each other both due to their instantaneous interactions at time t as well as the collective memory of the past trajectories $t' < t$. This historical dependence washes any symmetry from the initial condition of the monomer positions and orientation in the chain. In absence of historical chemical interactions, the chain will preserve the initial symmetry in the steady-state dynamics. Naturally, this requires τ_c to be much smaller than other deterministic time scales τ and τ_f , which is the case in phase IV+. In the absence of such a dominant τ_c - there is no historical buildup of the chemicals - we get phase III+, where no such universality is seen. This history-dependence of the dynamics distinguishes this model (see also [18, 20]), from other chemically interacting colloidal models [34–37], where instantaneous chemicals are assumed to be deposited on the surface.

IV. AN ACTIVE CHAIN OF CHEMO-ATTRACTIVE MONOMERS

We now turn to the case of chemo-attractive monomers with $\chi_r < 0$. The Υ matrix here has the form $\Upsilon_{ij} = -1 \quad \forall i, j$. Here, the monomers will preferentially point *towards* each other upon sensing the chemical field. We report a colloidal crystallization mechanism [1, 19, 38–40] where the long-ranged attraction renders the initially propelling chain to undergo a collapse onto itself thereafter remaining quasi-stationary (see SI Videos 3, 5 [33]).

A. Metastable crystallites for $N < 8$

We first distinguish two separate cases of collapsed chains, which we call (i) *metastable crystallites*, and (ii)

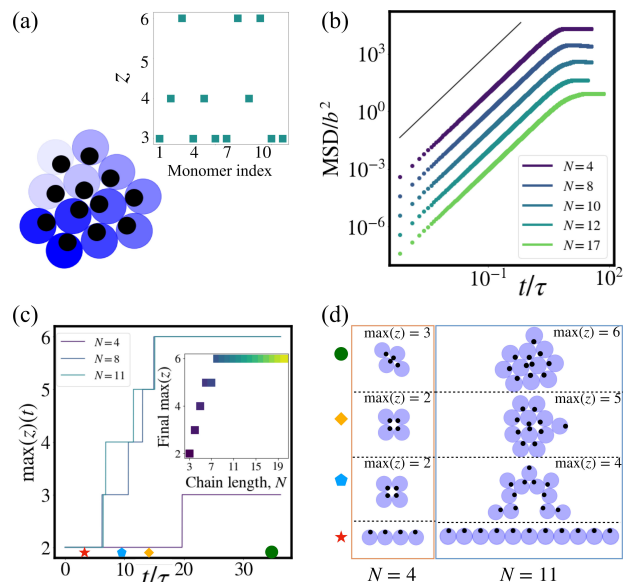


FIG. 4. Chemo-attractive results: distinguishing metastable and hexagonally packed states. Panel (a) displays an example of a hexagonally-packed crystal. The colors are shaded such according to monomer number, with the vertically most upward being the lightest. The coordination number for the configuration is shown in the inset, with the central three ($z = 6$), edge ($z = 4$) and vertex ($z = 3$) monomers displayed. In (b), the MSD is plotted (for $N = 4, 8, 10, 12$, and 17), where the halting of motion is seen at $t \sim 10\tau$. In (c), examples of the time evolution of our packing order parameter $\text{max}(z)(t)$ is shown for $N = 4, 8$, and 11 , to distinguish between metastable the lattice of $N = 4$ and the remaining two hexagonal packing. The former has a long lived transient lasting $O(10^1)\tau$, whilst the latter has much short-lived transients, eventually reaching $\text{max}(z) = 6$. In the inset, the final value is shown, showing that $\text{max}(z) = 6$ is attained from $N = 8$ onwards. For the time points labelled in the bottom of (c), the snapshots of the packing are displayed in (d), for $N = 4$ (left) and $N = 11$ (right). In particular, the final packed crystals have no positional spacing in between next-nearest neighbouring monomers, which can be seen for $N = 4$ of the first and second from bottom rows, and $N = 11$ for the first from bottom row.

hexagonally packed crystals. The former is characterized by long-lived (typically $\sim 10^1 - 10^2\tau$) transient metastable crystals (either propelling or stationary depending on net \mathbf{P}) that collapse onto other crystal within the time scale of simulation, whilst the latter does not display any such transient states (any transients here collapse within a time less than $O(\tau)$).

To distinguish these two types of crystals, we define a *coordination number* (z) for each monomer

$$z = \{|\mathcal{N}_i|, \forall i\}, \quad \mathcal{N} = \{|\mathbf{r}_i - \mathbf{r}_j| < 2b, \forall j \neq i\} \quad (14)$$

with the $\text{max}(z)$ being an order parameter used to distinguish different steady-state configurations. For all chain lengths N , the steady-state crystals are close-packed structures, such that each monomer has $z \geq 2$.

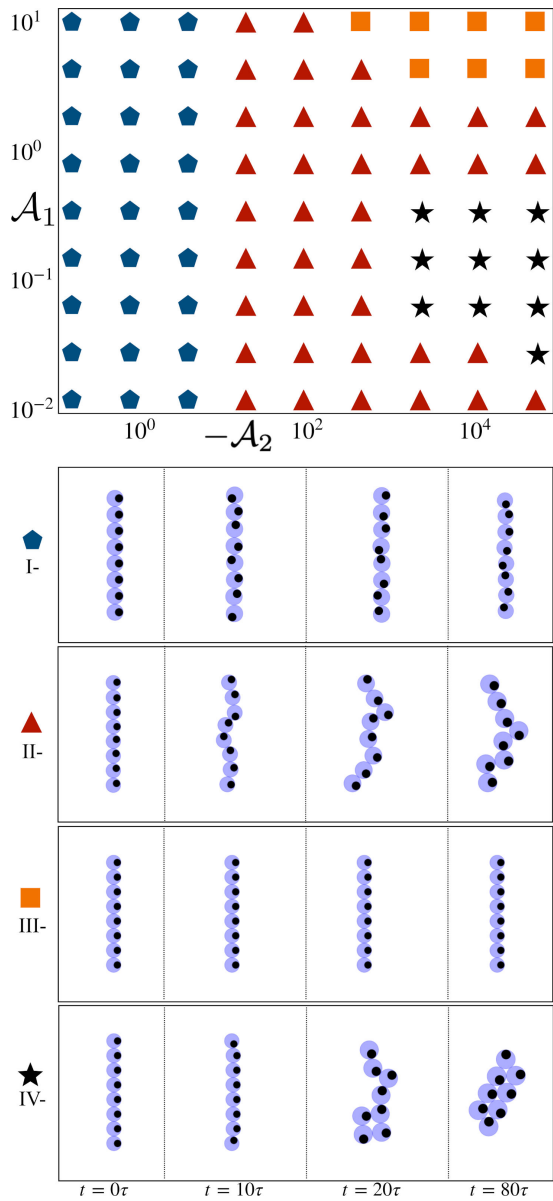


FIG. 5. Phase diagram for the chemo-attractive case. The four states are: (i) I-: Stiff + stationary chain, (ii) II-: FJC-like dynamics, (iii) III-: Stiff+propelling state, (iv) IV-: closed packed lattice. Parameters used for $(\mathcal{A}_1, \mathcal{A}_2)$ are (i) $(10^{-1}, 10^{-1})$, (ii) $(\mathcal{A}_1, \mathcal{A}_2)$ are (i) $(10^{-1}, 10^1)$, (iii) $(10^1, 10^3)$, (iv) $(10^{-1}, 10^4)$. Phase diagram is constructed for $N = 8$.

For chains of $N \geq 8$, this is identified by $\max(z) = 6$ (hexagonal packing). For $N < 8$, we in turn have the metastable crystallites. An example of this is shown in Fig. 4(d), with the left panel displaying the packing evolution of the $N = 4$ chain, whilst the right panel displaying $N = 11$. For the former, we see that the metastable “square” structure, with $\max(z) = 3$, exists at times $t = 10\tau$ and $t = 13\tau$ (top panel *second* and *third* columns, eventually closing into a “cone” structure, with $\max(z) = 3$, at $t = 35\tau$ (*right* column). This metastable crystal is captured via the time evolution of $\max(z(t))$ in

Fig. 4(c), with only a discrete change in $\max(z(t))$ seen, corresponding to the “square-to-cone” transition. The behaviour for hexagonally packed crystals are markedly different, as is also seen in Figs. 4(d) ($N = 11$) and 4(c) ($N = 8$ and $N = 11$). In particular, we see that any transient lattices do not last longer than a few τ , before packing into a more close-packed structure, eventually forming the crystal.

Note that in theory $N = 7$ permits hexagonal packing, though in our simulations this occurs for selected realizations of noisy simulations ($D_r > 0$), or with carefully selected initial conditions that deviate from (A1). Thus, we do not study this hypothetical packed crystal any further. Videos of the collapse dynamics of the metastable crystallites are shown in SI Video 4 [33]. These crystallites are studied in more detail in Appendix C.

B. Hexagonal packing

An example of a hexagonally close-packed crystal is shown in Fig. 4(a) for $N = 12$. As a rule, either monomer on the edges of the initially straight configuration appear on the rim of the packed crystal. The specific set of z for this $N = 12$ configuration is shown in the inset, where the monomer set with $z = 3$ correspond to those in the rim and part of a pair-vertex, the pairs being (in monomer index units) $(1, 4)$, $(7, 8)$, and $(11, 12)$. Those with $z = 4$ correspond to rim plus edge monomers, i.e neighbouring the vertex monomers on the same edge, whilst those with $z = 6$ correspond to the inner monomers. Apart from that, the exact configuration of packing varies significantly with (among others) χ_r . For instance, larger χ_r (thus larger l_r that promotes folding stronger at the edges, since deterministic rotation dominates over longer length scales of the chain (versus propulsion) - see SI Video 5 [33]). We do not study any further the monomer distribution of the packed structure as a function of these parameters as part of this study.

The dynamics of these structures display a quasi-halting of motion. This happens since the instantaneous $\dot{R} \propto |\mathbf{P}|$, and for the hexagonally packed structures $|\mathbf{P}|$ is vanishingly small for large N (all monomers point towards each other), and so the final collapsed state will be quasi-stationary, with a marginal drift along \mathbf{P} . The halting of the chain is seen via the MSD in Fig. 4(b), where a plateau is seen, which was absent in the chemo-repulsive case (with the exception of $N = 2$). This occurs at $t \sim 10\tau$, corresponding to the point of $\max(z) = 6$ in Fig. 4(c). The net polarization of this packed lattice is found to be of $\sim 10^{-2}$, with U of the final crystal at most 1/10th the minimum U of the chemo-repulsive case. Movies of various packing sequences are shown in SI Video 5[33].

C. Phase diagram

We can repeat the same procedure as done in the previous section and obtain the phase diagram for the chemo-attractive system; here, we use $\max(z)$ (maximum coordination number) to distinguish the different phases. This is shown in Fig. (5). It is qualitatively similar to that in Fig. (2), and thus we have identically labelled the phases as I-, II-,III-, and IV-, where the aforementioned relative dominance of relevant length and time scales in each of the phases are identical. The region IV- differs from IV+ in that they now describe a collapsed lattice structure. Further, the line delimiting phases IV and II for large \mathcal{A}_1 (the *weakly interacting* region) if shifted, such that large \mathcal{A}_1 and large \mathcal{A}_2 (e.g. $(\mathcal{A}_1, \mathcal{A}_2) = (10^3, 10^{-2})$) does not crystallize. We expect that a similar trend to be seen for the chemo-repulsive case if values $\mathcal{A}_1 \ll 10^{-2}$ are probed - i.e no stable C-configuration when the system is weakly interacting since there are no discernible concentration gradients in the system. Phases II+ and II- are also qualitatively different, in that in the latter case, one sees more distinct ‘‘FJC-like’’ behaviour, with the chain collapsing and relapsing on itself (see SI Video 3 [33]), compared to II+ where there is no collapse as such. Movies of the chemo-attractive phases are in SI Video 4 [33]. Rotational diffusion has previously been argued to drive crystal break-up and re-arrangement [38] in activity-driven aggregation [1, 41], and we see a chain analogue of this in this phase. In addition, we have also measured in the MSAD (not shown in this paper), where, unlike in the chemo-repulsive case, there is no stiffening with larger N , by reason of its collapsed configuration.

V. AN ACTIVE CHAIN WITH BINARY MIXTURE OF CHEMO-ATTRACTIVE AND CHEMO-REPULSIVE MONOMERS

We next turn our attention to a binary mixture system, where two species A and B populate the chain. Next, we focus on the case where the two-species interact in a non-reciprocal fashion, such that (for instance) A chases B, whilst B is repelled from A.

Such non-reciprocal interactions are known to be present in (isolated) colloidal systems [42–46], and have been studied theoretically and computationally in various particle-based [35–37]; field-theoretic [47, 48], and continuum solid [49–51] models. Our study here is distinct in that apart from non-reciprocity of chemical interactions [36, 47–49], our constituent units are themselves polar self-propelling particles (i.e non-reciprocity here does not by itself drive the system out of equilibrium). We will observe a wide range of phenomenology, many of which we believe are hitherto unreported in such systems.

In this Section, we will also study the dynamics of monodisperse dimers from the previous Sections III and IV (i.e. the AA and BB configurations) - this will help

in contrasting with results of the AB configuration. We first study *dimers* of configurations AA, BB, and AB; and later proceed to the study of trimers. In the later case, we will show that the breaking of action-reaction symmetry in the monomer interactions lead to emergence of states that display various phenomena at the collective level: chirality, undulatory gaits and direction reversal.

For the rest of this section, we will denote AB+(-) and that where species A is attracted to (repelled from) species B. For the entirety of this section, we study the noiseless case with sufficiently diffuse chemicals ($D_r = 0$, with $\tau_c \ll \tau$, i.e in the Phase IV regime). A full study of the different phases for dimers and trimers are not carried out here, though we expect the results to be qualitatively similar to those in the previous section.

A. Dimers - single species

For the single species dimers, we have shown in Fig. (3) previously that the dimers (AA) come to a halt (see SI video 2 [33]). This is seen in the polar plot of Figure 6(b), where we see the initially vertical orientations reach the fixed points for $\theta_1^* = \frac{\pi}{2}$ and $\theta_2^* = -\frac{\pi}{2}$. This is also true for the BB configuration; this is shown in Fig. 6(a) (*top row*) and the polar plot of Fig. 6(b), where now $\theta_2^* = \frac{\pi}{2}$ and $\theta_1^* = -\frac{\pi}{2}$. The orientational fixed points are thus

$$\mathbf{e}_1^* = \begin{pmatrix} 0 \\ 1 \end{pmatrix}, \quad \mathbf{e}_2^* = \begin{pmatrix} 0 \\ -1 \end{pmatrix}. \quad (15)$$

For the BB configuration the fixed points are the opposite

$$\mathbf{e}_1^* = \begin{pmatrix} 0 \\ -1 \end{pmatrix}, \quad \mathbf{e}_2^* = \begin{pmatrix} 0 \\ 1 \end{pmatrix} \quad (16)$$

with its dynamics displayed in Fig. 6(a) (*second row*) and the polar plot of Fig. 6(c). We see that the AA and BB configurations are completely symmetric to one another.

We can use Eq. (15) to show that the dynamics of both AA and BB come to a halt. To this end, we have after adding Eq. (1) for both species,

$$\frac{d \sum_i \mathbf{r}_i}{dt} = v_s \sum_i \mathbf{e}_i^* + \mu \sum_i F_i = v_s = v_s \sum_i \mathbf{e}_i^* \quad (17)$$

In the above we have used that fact that for $N = 2$, $\mathbf{J}_1 = -\mathbf{J}_2$ (rendered via the symmetries given in (B4), and for any N the spring forces sum to zero. Thus, $\sum_i \mathbf{e}_i^* = 0$, which implies that $\dot{\mathbf{R}} = 0$. Thus, we arrive at the result that the CM motion is static.

B. Dimers - AB

We now turn to the case of non-reciprocal dimers, where we uncover an ‘‘alignment chasing’’ behaviour.

Such two-species chasing has been reported in previous studies of colloidal models (far-field interaction with short ranged chemicals [35], field-theoretic models [47, 48], and prey-predator models [52, 53]). Thus, the alignment chasing reported here extends this phenomenon to an active colloidal chain in a straightforward manner. For the dimer-AB, the matrix entries for Υ_{ij} are given by:

$$\Upsilon_{ij}^{AB} = \delta_{i1} (\delta_{j1} - \delta_{j2}) - \delta_{i2} (\delta_{j2} - \delta_{j1}). \quad (18)$$

We see that in the case of an AB-dimer, the action-reaction symmetry can be broken in two distinct ways [AB(+) and AB(-)]. We study both these cases below.

The results for the AA and BB configuration are shown in Figure 6(a) and (b) respectively. AB+ configuration are shown in Figure 6(c), whilst the AB- configuration is in 6(d). We see that in both AB+ and AB- cases, the monomers quickly settle on a solution where they are mutually aligned (having the same orientation) and self

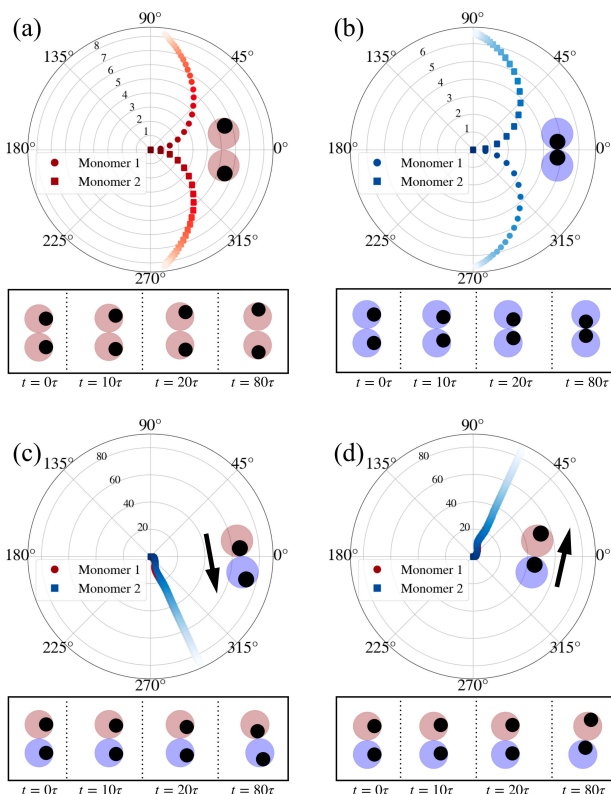


FIG. 6. Dynamics of dimers for AA, BB and AB cases. Polar plots of the dynamics are displayed in panels (a) - (d). The radial axis of these plots indicate distance, $|\mathbf{R}_i(t)|/b = \sqrt{x_i(t)^2 + y_i(t)^2}/b$, from the origin, angular axis indicates orientation for each monomer (using convention given in Appendix A). The trajectories are color shaded according to time - from darkest (initial) to brightest (final). Inset indicates snapshot of steady-state dimer, with accompanying arrow showing its propulsion direction (no propulsion for AA and BB dimers in the steady-state). Each panels also displays snapshots at $t = 0, 10\tau, 20\tau$, and 80τ .

propel in a chasing behavior (see SI video 7 [33]).

This chasing result is also straightforwardly deduced analytically. Considering the attractive AB interaction, we have that the fixed point for $\dot{\mathbf{e}}_{1A} = 0 \implies \mathbf{e}_{1A} \propto -|\chi_r|(\mathbf{r}_{1A} - \mathbf{r}_{2B})$. On the other hand, $\dot{\mathbf{e}}_{2B} = 0 \implies \mathbf{e}_{2B} \propto +|\chi_r|(\mathbf{r}_{2B} - \mathbf{r}_{1A})$. Thus, we note that \mathbf{e}_{1A} is parallel to \mathbf{e}_{2B} . This happens after about $t \sim 80\tau$ of the dynamics (see Fig. 6(a), *bottom row*). On the other hand, the dynamics at the fixed point in the phase space of $\{R_x, R_y\}$ read

$$\frac{dR_x}{dt} = 2v_s \cos(\theta^*), \quad \frac{dR_y}{dt} = 2v_s \sin(\theta^*) \quad (19)$$

after which the dimer propels indefinitely along a fixed angle θ^* which we can also deduce. The steady state angle the dimer picks is $\approx 292.5^\circ$, half way in between that of a full vertically downward chase ($\theta = 270^\circ$), and an unbiased diagonal $\theta = 315^\circ$, owing to the symmetry of the problem. For the AB(+) case, the same argument gives the steady-state angle as $\approx 67.5^\circ$.

Let us summarize the results for dimer interactions. The monodisperse dimers (both AA and BB) come to a halt, whereas the bidisperse dimers propel at a fixed angle, one species chasing the other indefinitely. The reduced phase space is 3 dimensional for the monodisperse dimers *throughout* the dynamics (see Appendix D). For the AB molecules, the reduced phase space is also 3 dimensional, whilst it is 1 dimensional *at the fixed point orientations*, corresponding to a stably propelling dimer. With this, we now move on to the trimer cases.

C. Trimers: oscillations, swimming, and reversal of motion due to breaking of action-reaction symmetry

Having established that dimers perform deterministic chase, we now study the trimer chains, specifically the configurations of ABA, BAB, and BBA. We uncover striking consequences as a result of this additional degree(s) of freedom of the trimer. In particular, chasing as in the previous section is now extended to an undulatory gait for BBA(-) and AAB(+), and in addition we will obtain coupled oscillations of “tail” monomers for ABA(-). Finally, we will see that BAB(-) *reverses* its direction of motion.

For these configurations, the matrix entries for Υ_{ij} are given by:

$$\Upsilon_{ij}^{ABA} = (\delta_{i1} + \delta_{i2} + \delta_{i3}) (\delta_{j1} - \delta_{j2} + \delta_{j3}) \quad (20a)$$

$$\Upsilon_{ij}^{BAB} = -\Upsilon_{ij}^{ABA} \quad (20b)$$

$$\Upsilon_{ij}^{BBA} = (\delta_{i1} + \delta_{i2} + \delta_{i3}) (-\delta_{j1} - \delta_{j2} + \delta_{j3}) \quad (20c)$$

We further quantify the dynamics by the bond angle ϕ of the trimer. This uniquely specifies the relative monomer positions for the ABA and BAB configurations.

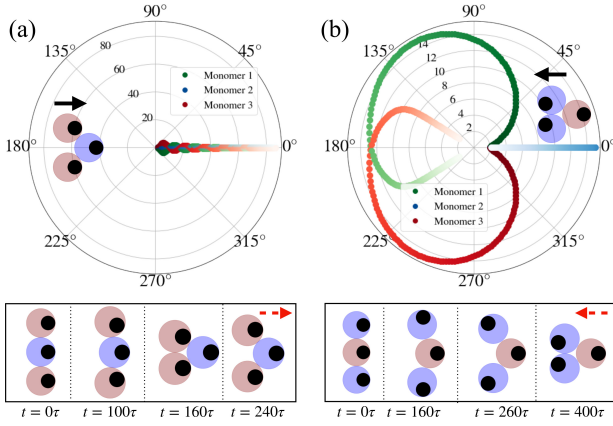


FIG. 7. Dynamics of trimers, ABA(-) and BAB(-), with chemical affinities that break the action-reaction symmetry. Panels (a)-(b) on top row display polar plots for ABA(-), BAB(-) respectively. Black arrow indicates direction of $\dot{\mathbf{R}}$. The bottom panels show the snapshots from simulations for the corresponding cases. Red dotted arrow on right most snapshot indicates net polarization direction.

We define an “angular momentum” of the system

$$L_z = \frac{1}{N} \sum_i^N \left(\mathbf{v}_i \times (\mathbf{r}_i - \mathbf{R}) \right) \cdot \hat{\mathbf{z}} \quad (21)$$

which quantifies net rotations of the monomers about the center of mass (for a 2D system there is only one such component projecting out of plane of the page).

The results are displayed Fig. (7) and Fig. (8). The dynamics of ABA(-) trimer is shown in Fig. 7(a). The ABA(-) trimer displays oscillatory angular dynamics, since the edge A monomers are repelled from the center and are equally repelled from each other. They eventually stabilize at an angle of $\phi \approx 105.9^\circ$, as shown in Fig. 8(d) (blue curve). For ABA and BAB where the interactions are symmetric, ϕ can be shown to uniquely specify the dynamics, and that the effective system lies in $\{\phi, \theta_1\}$. We get (see Appendix(E)):

$$\dot{\phi} = \frac{v_s}{2b} \sin(\theta_1) \sec\left(\frac{\phi}{2}\right) \quad 0 \leq \phi < \pi \quad (22)$$

Thus, the bond angle stabilizes when $\theta_1 = 0$ as in the ABA case (Fig. 7(a)).

Similar to the procedure outlined in the previous section, the dynamics of the ABA(-) can be reduced $\{x_1, x_2, y_1, y_2, e_{x_1}, e_{x_2}, e_{y_1}, e_{y_2}\} \rightarrow \{R_x\}$ at the *fixed point* (see Appendix (E)),

$$\frac{dR_x}{dt} = v_s \left(2 \cos(\theta_1^*) + \cos(\theta_2^*) \right) = 3v_s \quad (23)$$

thus the stable propelling trimer is analogous to Eq. (19) with a proportional propulsion speed.

The dynamics of BAB(-) configuration is shown in Fig. 7(b). We see that the trimer *reverses* its direction. The cardioid-resembling polar trajectory plateaus

at $|R(t)| \approx 14b$, after which the trimer reverse in direction, eventually reaching the origin. The mechanism for this is clear - the edge B monomers are repelled from the central A but are mutually attracted to one another. The equation governing the fixed point propulsion analogous to Eq. (23) is

$$\frac{dR_x}{dt} = v_s \left(1 + 2 \cos(\theta_1^*) \right) \quad (24)$$

Noting that $\theta_1^* \approx \pi$ (Fig. 7), we see that the center of mass propels in the -ve x direction. This “reversal time scale” can be tuned by setting $\frac{\tau_f}{\tau}$ accordingly (for large $\frac{\tau_f}{\tau}$ the system will reverse quicker). The steady state ϕ of the trimer is straightforwardly given by $\frac{\pi}{3}$ (close packed), which we see in Fig. (7). Movies for the ABA and BAB configuration are in SI Videos 8 and 9[33].

Finally, we have the result for the BBA(-) configuration in Fig. 8(a) (see SI Video 10 [33]). We see an emergent undulatory gait motion, reminiscent of a microswimmer [54]. The behaviour is driven by a competition for alignment between the tailing A and the central B monomer. After an initial transient, the system settles into an oscillatory state, which lasts indefinitely within the time scale of the simulation. This oscillatory behaviour is characterised by limit cycles in phase space, as is shown in Fig. 8(c). On the top panel, we see that both θ_3 and θ_1 are independently coupled to θ_1 . On the bottom panel, we see that, as a consequence, the relative coordinates $\mathbf{x}_1 - \mathbf{x}_2$ and $\mathbf{x}_1 - \mathbf{x}_3$ are coupled. The oscillations are captured by ϕ and L_z (21) - see Fig. 8(d) and (e). In particular, L_z differentiates BBA(-)’s dynamics with the other configurations, as undulations give rise to time-periodic oscillations in both bond angle and an angular momentum w.r.t center-of-mass.

Such temporal periodic waves have also been reported in other non-reciprocal models of active matter [47–49, 51], with the key difference being that in these the activity arises purely due to the non-reciprocity, with the systems otherwise being in equilibrium. Our travelling states (propagated via the BBA body) here are thus driven by *both* the polar nature of the chain and the underlying anti-symmetric chemical interactions. These self-sustained gaits could also hint to a simple “chemotactic gait” mechanism for microorganism swimming without the need to recourse to hydrodynamics [55, 56], and/or mechanical models [57]. Swimming gaits here arise purely due to competing chemotactic mechanism and are self-sustained via the non-linearities of the chemical trails in (5).

We note that there are two other configurations for the trimer case. The results for these three cases: ABA(+) and BAB(+) are shown in Appendix (F). Finally, we also have a validity of our scaling relation (12) for the ABA and BAB configurations, owing to their symmetric histories of the trajectories (see Appendix (E)). This is displayed in Fig. 8(f).

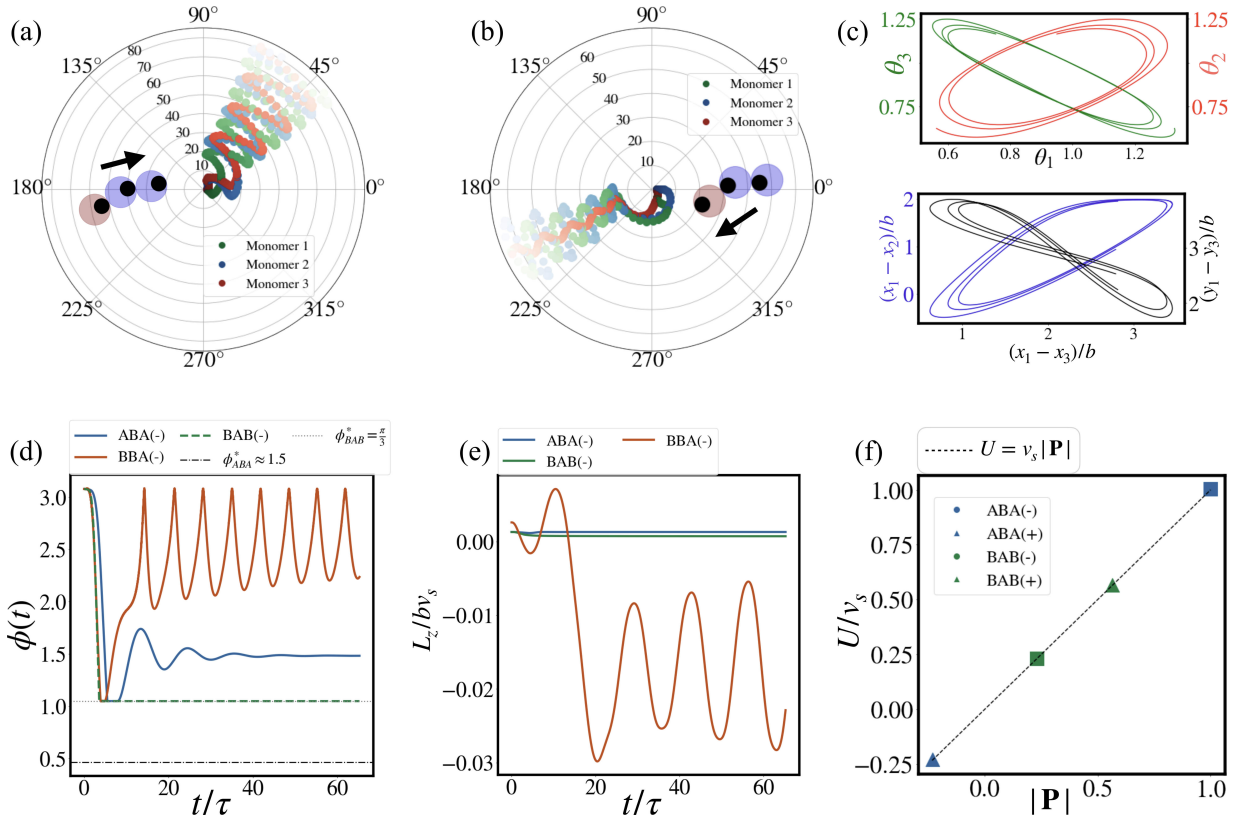


FIG. 8. Self-sustained undulatory gaits of the BBA trimer due to anti-symmetric chemical affinities. Panel (a) and (b) display polar plots for the dynamics of BBA(-) and BBA(+) trimers respectively. Panel (c) displays the underlying attractor with the coupling of head and middle orientations to the tail (*top*) and (hence) a coupling in the reduced coordinate space of $(x_1 - x_2, x_1 - x_3)$ and $(y_1 - y_2, x_1 - x_3)$ (for BBA(-)). Note that shared y-axes are used here, the respective quantities are colored same in the plot as in their axis labels. Panel (d) displays both $\phi(t)$, quantifying bond angle dynamics of configurations. Vertical dotted lines indicate steady-state ϕ attained by respective configurations. Panel (e) L_z , capturing the undulation of BBA versus the other two. In (f) validation of (12) is shown for ABA(-),BAB(-),ABA(+), and BAB(+) configurations (excluding the BBA configurations).

VI. CHIRAL ACTIVE FOLDAMERS

The trimer results above hint to a broader design principle for active colloidal molecules: the ability to acquire specific steady-state structure and/or dynamics by carefully designing the interactions and/or initial conditions. For this section, we term our final collapsed structure as an *active foldamer* [14, 15]. In particular, our model straightforwardly produces *chirality* in the foldamer dynamics. The brief outline of the mechanism is as follows. For a monodisperse chain with a single segment, the foldamer consists of a single \mathbf{P} vector, passing through its center of mass. For foldamers of more than one species, each distinct segment of the chain has its respective $\mathbf{P}^{(\alpha)}$, but now each of the segment's $\mathbf{P}^{(\alpha)}$ no longer passes through the CM of the foldamer. As a result, rotations are induced which are proportional to the (perpendicular) distance of the $\mathbf{P}^{(\alpha)}$ vectors to the CM. For the rest of the segment we denote the segment indices as $\{\alpha_1, \alpha_2, \dots, \alpha_M\}$ for M generic segments. This mechanism can produce two phenomenon: (i) planar ro-

tation about a point in the case where the composite molecule has a non-zero net \mathbf{P} , and (ii) rigid body rotations about the molecule CM (“spinning”), if the net \mathbf{P} is (designed to be) zero. A generalized form of Eq. (21) gives the rotational frequency of the molecules $\frac{L_z}{b^2}$, with here $L_z = v_s \sum_{\alpha} \left(\mathbf{P}^{\alpha} \times (\mathbf{r}^{\alpha} - \mathbf{R}) \right)$. An example of the former is shown in Fig. 9 (a), which is a stable (elliptical) orbit for the B_7A_4 configuration (see SI Video 11 [33]). Here, there is a “nucleus” of B type being propelled by a “rim” of A type. The net handedness is clockwise. These dynamics are stable, in that the positions and orientations of the rotor do not change in the steady-state - i.e there is a fixed chirality in the system that stably persists. The inset of Fig. 9(a) shows the initial conditions of the B_7A_4 configuration; first two segments are identical to (A1), with $\theta_i^{\alpha_3} = \pi \quad \forall i$.

Constructing instead a foldamer that has a net zero polarization, but \mathbf{P}^{α} segments symmetrically away from the CM in opposite orientations, one can design dynamics that exhibit rotations about the foldamer CM - i.e. a spin degree of freedom. The simplest examples of these are

molecules with symmetrically located oppositely aligned \mathbf{P}^{α_1} and \mathbf{P}^{α_3} , along with a central segment of $\mathbf{P}^{\alpha_2} = 0$. Attaining such structures require a judicious choice of Υ_{BB} , Υ_{AB} , and Υ_{BA} entries; examples of these are indicated in the insets of Fig. 9. We report here two such foldamers, distinguished by the position of the ‘‘arm’’ segments with respect to the central body - i.e whether they are free or attached to the central body. We use the label Foldamer F1 for those that have ‘‘free-arm’’ segments of species A. The final collapsed structure is highly sensitive to the initial conditions. Labelling the length of the A-type arm segments as m , we obtain different structures for Foldamer F1 with variation in m - we label this with the prefixes (a)/(b) to distinguish the two Foldamer F1 structures. An example of Foldamer F1a is the $A_6B_6A_6$ configuration shown in Fig. 9(b). An example of Foldamer F1b is the $A_2B_6A_2$ configuration is shown in Fig. 9(c), with the initial conditions and Υ matrix shown in the inset (*left* and *bottom right*). For Foldamer F2, the A-type arms are attached onto the

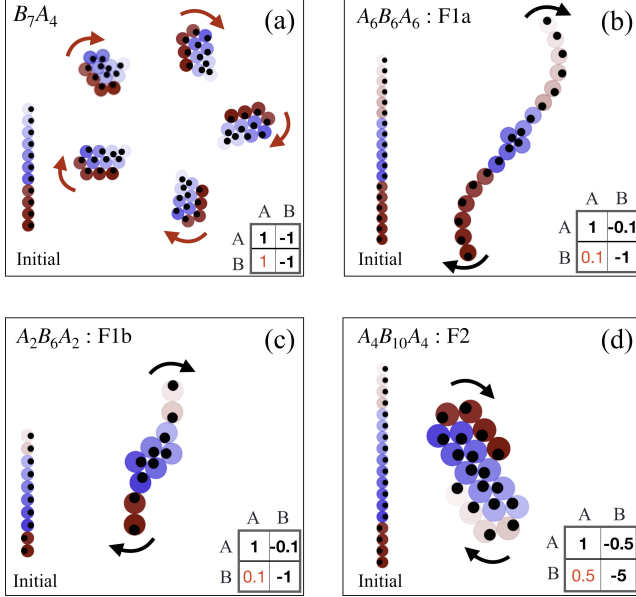


FIG. 9. Different types of chiral rotors. Panel (a) illustrates the stable rotations of the B_7A_4 molecule. Panels (b) and (c) illustrates the rotational dynamics for example cases of Foldamer F1a ($A_6B_6A_6$ configuration) and Foldamer F1b ($A_2B_6A_2$ configuration) respectively. These spinning molecules have free arm segments, that act as rotor blades. Panel (d) illustrates the Foldamer F2 rotational dynamics, characterized by attached arm segments, for the $A_4B_{10}A_4$ configuration. For all panels initial configuration is shown on the left, with Υ matrix entries in bottom right. Red curved arrows indicate instantaneous change propulsion direction, whilst black curved arrows indicates rotation about CM. For panels (b) and (c), $k_{sp} = 3.48 \times 10^4 \mu\text{m}/\text{s}^2$ and for panel (d), $k_{sp} = 1.74 \times 10^5 \mu\text{m}/\text{s}^2$. For all plots and insets, we use reddish color for A monomers and bluish color for B monomers. Color shading is to specify initial position along the chain.

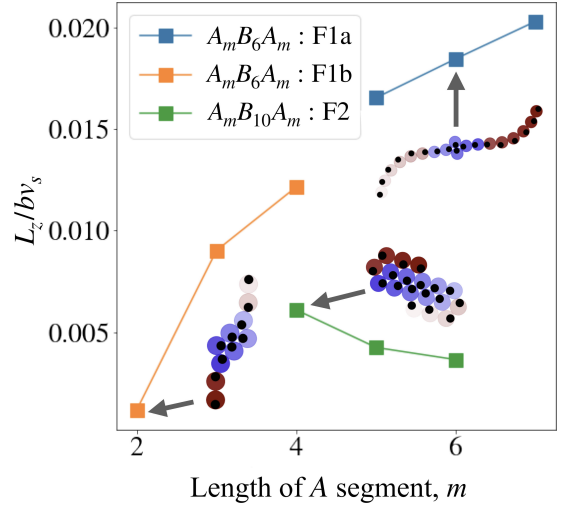


FIG. 10. Tunable rotational frequency of foldamers. Rotational frequencies (non-dimensionalized) of Foldamers F1 ($A_m B_6 A_m$) and F2 ($A_m B_{10} A_m$), $L_z/v_s b$, are plotted versus the length of the A type segments, m . Foldamers F1a and F1b are shown in blue and yellow, with Foldamer F2 in green. Insets show molecule corresponding to the m value indicated by the black solid arrow. Color scheme is same as in Fig.9.

B-type central body; an example of this is shown in Fig. 9(d) for the $A_4B_{10}A_4$ configuration (respective Υ matrix again found in inset).

The rotational frequency of these foldamers are thus straightforwardly seen to be determined by the contribution of the arm segments’ \mathbf{P}^α , and that they are *tunable* via variation of the length of the arm segments. This is shown in Fig. 10, with the rotational frequency $L_z/(bv_s)$ plotted against the length of the A arm segment, m . Foldamers F1 and F2 display different response in their rotational frequency to an increase in m , namely Foldamers F1 enhance their rotational frequency whilst Foldamers F2 *decrease* their frequency. For Foldamers F1, this occurs since $\mathbf{r}^\alpha - \mathbf{R}$ increases with m (in addition to the commensurate increase in \mathbf{P}^α - see Fig (3)). Movies of Foldamers F1a and F1b are shown in SI Videos 12 and 13 respectively [33]. For Foldamers F2, instead $\mathbf{r}^\alpha - \mathbf{R}$ decreases with m . We note that the range of m probed here instead is relatively narrow, only $m \in \{4, 5, 6\}$, since for $m < 4$ and $m > 6$ the structures change significantly (not shown in this paper). These indeed could be other classes of Foldamers by themselves, but we do not pursue the study of them any further. Movie of Foldamer F2 can be seen in SI Video 14 [33]. A longer range of m to display the tuning could in principle be done with a foldamer with a longer B body segment - we leave this to future work.

We have thus shown in this section that our model produces two distinct types of chirality in active foldamer dynamics, with the latter being tunable. The tunability can also be positive (increasing with segmental length) or negative depending on whether the foldamer has free

or attached arm segments. We clarify here that whilst the segmental polarization mechanism here is generically applicable for any interaction matrix between the distinct species, the spinning rotors that we observe seem to require a *non-reciprocity* in the species interactions (e.g. any composite molecule with arbitrary Υ will have dynamics that break handedness symmetry, but they may not acquire a spin degree of freedom).

VII. SUMMARY AND DISCUSSIONS

In summary, we have shown how a simple model of a chemically self-interacting colloidal chain can support a wide range of dynamical phenomenology, including rigid flocks, self-sustained undulatory gaits and chiral rotors. In particular, we have uncovered (i) the role of chemical trails in providing an sustained asymmetry in the dynamics, and (ii) the role of non-reciprocal (internal) alignment interactions in the collective dynamics, which in addition we have shown to be tunable. The former necessitates two particular phenomena reported here. Firstly, the universal C-shape rigidity in the chemo-repulsive chain. Here, the historical build-up of chemicals in (5) renders a forward-backward asymmetry in the dynamics of the chain, resulting in a universal C-shape flock (see SI Video 6 [33]). Without such an asymmetry, the C-shape acquisition ceases to be universal, and dependent solely on the initial conditions. Second, it gives rise to a self-sustained *chemotactic undulations* of a binary species colloidal molecule with tail, body, and head monomers [10, 54], that self-sustains its microswimmer gait without any hydrodynamics and/or biomechanics. The tail-head A-B alignment interaction is mediated via the respective collective memory of the past trajectories, which is necessary for the undulatory gait to sustain itself. These results thus also point towards a novel function of trail-dependence in the collective dynamics in active matter [18–20], namely that they sustain a *spatio-temporal* asymmetry in the dynamics (i.e. particular pattern may be universally selected due to the shared collective memory of the past) - which in our study manifests as a global polar order of the chain. The effect of hydrodynamics on this function remains an open question.

The results for our binary species chain with non-reciprocal chemical affinities (oscillations, reversal of direction of motion, undulatory gaits, chirality) hint towards design principles of active molecules, where the “structure-function” paradigm of self-assembly holds; an example of which we have reported are chiral molecules. Various other “structure-function” specific molecules are possible, however; for instance in SI Video 15 [33] we report the “nucleus + envelope” molecule, where a stable nucleus of species B is shielded with a rim of species A, with the overall molecule propelling stably in the positive x -direction. Extending this to multiple species, we envisage that our model can be used to program active dynamical features of colloidal molecules [15] via these

aforementioned parameters - interaction types, initial orientations, and segmental lengths; this will be pursued in a future work.

Chirality, as shown here, can exist in any generic multi-segment configuration, whilst a spin degree of freedom (rotations about the body CM) can be incorporated by a chemo-attractive body segment, and chemo-repulsive arm segments that are oppositely aligned. Connecting to biological systems, we note that chiral dynamics is a ubiquitously reported feature - for instance in MDCK cell assemblies [58, 59] and the actomyosin cortex-cell nucleus complex [60]. It is interesting to note that our model provides a clear mechanism for the chirality via the internal non-reciprocal nature of the chemical affinities in the dynamics of the chain, without resorting to any hydrodynamics [39, 51, 60]. The tunable nature of the rotational frequency of such molecules further suggest that such structures can be used as microscopic clocks; it would be interesting to see if biological systems apply similar time-keeping mechanisms for their function.

Extensions of this work could be the study of many interacting chains, where the effects of topological defects are imminent, as well as to 3D. In terms of connection to experiments, we note that at a modelling level, we have ignored hydrodynamic interactions. This is rationalised by the fact hydrodynamic fields decay more quickly than chemical fields in strong 2D confinement in Hele-Shaw cells, and thus do not affect our results significantly [27]. Experimental design of chasing interactions in colloids have been realized (e.g. in [46]), and our results thus provide testable predictions for phenomenon described here.

ACKNOWLEDGEMENTS

We thank Ronojoy Adhikari, Mike Cates, Vijaykumar Krishnamurthy, and Ignacio Pagonabarraga for useful comments. AGS acknowledges funding from the DIA Fellowship from the Government of India. ST also thanks the Department of Atomic Energy (India), under project no. RTI4006, the Simons Foundation (Grant No. 287975), the Human Frontier Science Program and the Max Planck Society through a Max-Planck-Partner-Group for their support. RS acknowledges support from seed and initiation grants from IIT Madras as well as a Start-up Research Grant from SERB, India.

Appendix A: Simulation details

We simulate Eq. (1) using a forward Euler-Maruyama method to evolve the positions and orientations of the particles in time. For the entire paper (unless specified

otherwise) we use the following initial conditions:

$$\theta_i(0) = 0, \quad x_i = 0, \quad \forall i \quad (\text{A1a})$$

$$y_{i+1}(0) = y_i(0) + 2b, \quad 1 \leq i \leq N-1 \quad (\text{A1b})$$

Here θ_i is the angle made by the orientation \mathbf{e}_i of the i th particle with the x -axis. Thus, Eq.(A1) implies that the initial chain is aligned vertically (upward facing in the plane of the page in this paper). In addition, we have observed that the results are universal and do not depend on the initial orientations (see SI Video 6[33]). A detailed study of the effect of initial conditions is not performed in this work. As mentioned in Section I, variation of translational noise is naturally important when considering the statistical mechanics of long ‘conventional polymer(s)’; here we instead study the precise *dynamics* of these chains. Indeed, using experimentally feasible quantities of $b \sim 25 \mu\text{m}$, viscosity of solvent $\eta \sim 10^{-3}$ [27], we find that the typical active force [$\mathcal{O}(6\pi\eta b v_s) \sim 10^{-11} \text{N}$], dominates the typical Brownian forces [$\mathcal{O}(k_B T/b) \sim 10^{-16} \text{N}$], and thus, D_t is ignored in this paper. D_r on the other hand, as we will show, plays a crucial role in the phase determination of the chain.

The model described in Section II has been numerically simulated in an unbounded two-dimensional (2D) space using a custom Cython code (Python on top of a C backend). Throughout the paper, we have used: $b = 25 \mu\text{m}$, $v_s = 50 \mu\text{m/s}$, $k_{sp} = 1.74 \times 10^4 \mu\text{m/s}^2$, $k_e = 8.70 \times 10^4 \mu\text{m/s}^2$, $c_0 = 1$ and $\chi_r = 7.5 \times 10^3 \mu\text{m}^3/s^2$. For the chemo-repulsive case (Figures 2, 11), $dt = 0.01$. For the chemo-attractive and binary species cases (Figures 4, 12, 5, 6, 7, 8, 14) $dt = 0.0018$. Unless varied (as in Figures 11, 12) $D_c = 2500 \mu\text{m}^2/s$, $\mathcal{A}_1 = 10^{-2}$, $\mathcal{A}_2 = 0$ (with $D_r = 0$). For all sections $\frac{\chi_t}{\chi_r} = 10^{-4}$, with the exception of Section VI (Fig 9), where $\frac{\chi_t}{\chi_r} = 10^{-2}$.

Appendix B: Dimensionality reduction from the symmetries of the dynamical system

To write down reduced dynamical equations for dimers and trimers, one has to reduce the dimensionality of the phase space. In this section, we will outline the dimensionality reduction procedure that gives the generic relation Eq. (12), along with reduced dynamics of (19), (23), (24). To prove Eq.(12), as an instructive case, let us consider the time trajectory of the $N = 5$ chain, shown in Fig. (11)(a). The dynamics can be seen to be fully symmetric about the central monomer, and the following equalities can be deduced

$$y_1(t) - y_2(t') = y_4(t') - y_5(t) \quad (\text{B1a})$$

$$y_1(t) - y_3(t') = y_3(t') - y_5(t) \quad (\text{B1b})$$

$$y_2(t) - y_3(t') = y_5(t') - y_4(t) \quad (\text{B1c})$$

and further

$$x_1(t) = x_5(t), \quad x_2(t) = x_4(t), \quad \forall t \quad (\text{B2})$$

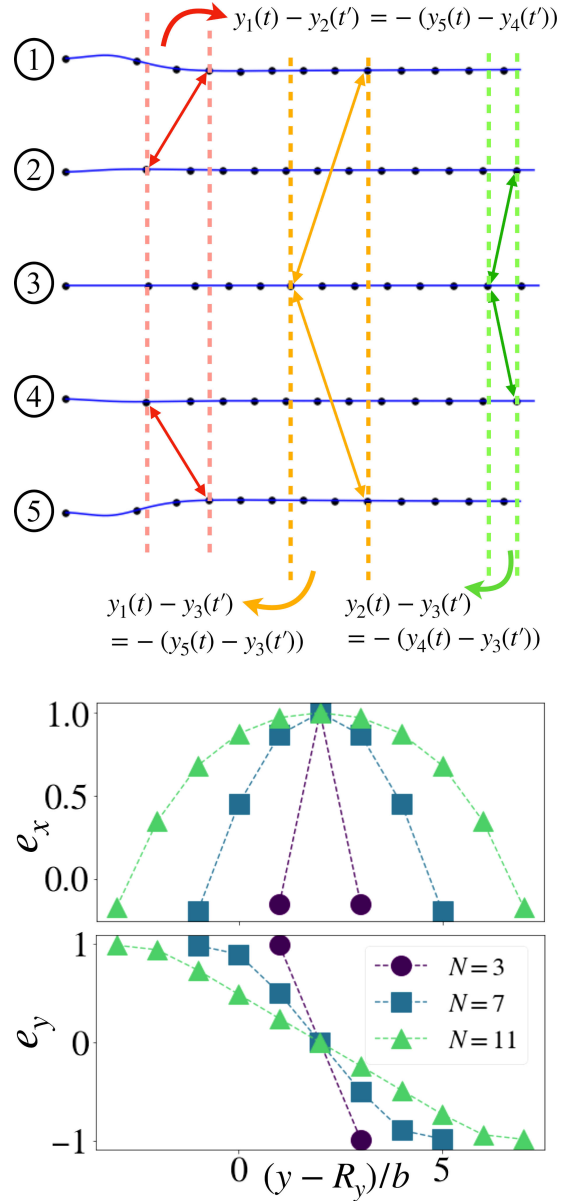


FIG. 11. Illustration of the symmetry of the dynamics for the chemo-repulsive case of $N = 5$. TOP PANEL: trajectory of each monomer in the chain is shown (labelled on the left), with time points colored in black. The equalities in (B1) can be deduced by taking vertical distances at different time points (a particular (t, t') pair is uniquely coloured). Equalities of (B2) is deduced by considering the time spacings. BOTTOM PANEL: steady-state orientations (e_x and e_y) satisfying Eq. (B4) are shown, for $N = 3$, $N = 7$, and $N = 11$. Dotted lines are a guide to the eye.

This symmetry, as we show in Appendix (B 1), allows us to show that the fixed points of the orientations are symmetric in one and anti-symmetric in another direc-

tion:

$$e_{x_1} = e_{x_5}, \quad e_{y_1} = -e_{y_5} \quad (\text{B3a})$$

$$e_{x_2} = e_{x_4}, \quad e_{y_2} = -e_{y_4} \quad (\text{B3b})$$

$$e_{x_3} = 1, \quad e_{y_3} = 0 \quad (\text{B3c})$$

For an arbitrary chain of N monomers, this generalizes to the condition:

$$e_{x_i} = e_{x_{N-i+1}}, \quad e_{y_i} = -e_{y_{N-i+1}}, \quad \forall i \in \{1, 2, \dots, N\} \quad (\text{B4})$$

Thus, a spatial symmetry in the problem implies an orientational symmetry. Note also that for odd-numbered chains, (B4) implies that $(e_x, e_y) = (1, 0)$ for the monomers in the (arithmetic) center. This symmetry is shown in Fig. (11b), where the orientations are plotted in the CM frame perpendicular to the propagation direction, in the continuum parametrization, showing that $e_x(y - R_y) = e_x(-(y - R_y))$, (*top panel*) and $e_y(y - R_y) = -e_y(-(y - R_y))$ (*bottom panel*) (the relation between the two given straightforwardly by $e_y = \sqrt{1 - e_x^2}$). Note that this straightforwardly implies that $\theta(-y) = -\theta(-(y - R_y))$. Summing up Eq. (1) across the chain, and using Eq. (13), we obtain Eq. (12).

We will show, in this and the following sections, that the scaling of Eq. (12) holds true *whenever* the symmetries in (B1) and (B2) are applicable (for instance during a certain duration of the dynamics). We will also show in Sections (V) that these symmetries can reduce the dimensionality of the system for dimer and (selected) trimer configurations. We also note that this scaling also holds true for arbitrary initial conditions not given by Eq. (A1) [27]. In this case, (12) does not apply throughout the dynamics, but merely in the *steady-state*, when the chain acquires the C shape (irrespective of the initial condition) that characterizes in phase IV+.

1. Derivation of orientational fixed point symmetry

We derive here the condition for the orientational fixed points for a representative $N = 5$ case, given by (B3). This is shown in Fig. (11). From (2), note that the orientational fixed points are reached if $\mathbf{e}_i^* \propto \mathbf{J}_i$. Let us define

$$\Delta x_{ij}(t, t') = x_i(t) - x_j(t') \quad (\text{B5})$$

$$\mathcal{F}_{ij}^{(x)}(t, t') = \exp \left[-\frac{[x_i(t) - x_j(t')]^2}{\mathcal{D}(t, t')} \right] \quad (\text{B6})$$

and likewise for $\Delta y_{ij}(t, t')$, $\mathcal{F}_{ij}^{(y)}(t, t')$ by the substitution $x \rightarrow y$. Then, using (5), we have:

$$e_{x_i}^* \propto \int dt' \sum_{\substack{j=1 \\ i \neq j}}^N \left[\frac{\Delta x_{ij}(t, t')}{\mathcal{D}(t, t')} \mathcal{F}_{ij}^{(x)}(t, t') \right]. \quad (\text{B7})$$

The symmetries given by (B2) renders

$$\Delta x_{1i} = \Delta x_{5i} \quad \Delta x_{2i} = \Delta x_{4i}, \quad \forall i \quad (\text{B8})$$

we thus see straightforwardly that $e_{x_1}^* = e_{x_5}^*$ since $\Delta x_{12} = \Delta x_{52}$, $\Delta x_{13} = \Delta x_{53}$, $\Delta x_{14} = \Delta x_{54}$, and $\Delta x_{11} = \Delta x_{55}$. Now using $\Delta x_{22} = \Delta x_{44}$, $\Delta x_{23} = \Delta x_{43}$, $\Delta x_{24} = \Delta x_{44}$, and $\Delta x_{21} = \Delta x_{41}$, we have $e_{x_2}^* = e_{x_4}^*$. Since this is an odd-numbered chain e_{x_3} takes a stand-alone value. We can show this to be 1 by finding $e_{y_3}^*$, instead of explicitly evaluating the integrals. This proves the x component of (B3). For the y component, we can repeat the procedure with $x \rightarrow y$ substitution in (B7). Using (B1), we get

$$\Delta y_{12} = \Delta y_{54}, \quad \Delta y_{13} = \Delta y_{53} \quad (\text{B9})$$

$$\Delta y_{14} = -\Delta y_{52}, \quad \Delta y_{14} = -\Delta y_{51} \quad (\text{B10})$$

$$\Delta y_{21} = -\Delta y_{45}, \quad \Delta y_{23} = -\Delta y_{43} \quad (\text{B11})$$

$$\Delta y_{24} = -\Delta y_{42}, \quad \Delta y_{25} = -\Delta y_{41} \quad (\text{B12})$$

which implies that $e_{y_1} = -e_{y_5}$, $e_{y_2} = -e_{y_4}$ from (B7). To prove that $e_{y_3} = 0$, we use

$$\Delta y_{31} = -\Delta y_{53} \quad \Delta y_{23} = -\Delta y_{32} \quad (\text{B13})$$

which completes the proof of (B3). ($e_{y_3} = 0 \implies e_{x_3} = 1$) For an arbitrary N , these results generalize straightforwardly to (B4). For odd numbered chains, the middle monomer always has $e_x = 1$, $e_y = 0$.

Appendix C: Metastable crystallites' symmetric histories

In this section we analyse the metastable crystallites. Let us call the time at which the metastable crystallites lose their stability as the *collapse time*. We can again exploit the symmetric histories argument, which we find to

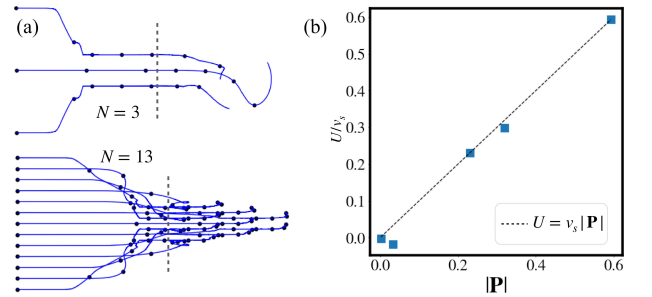


FIG. 12. Metastable crystallites in the chemo-attractive case, demonstrating range of validity of the symmetric-trails approach. In (a) *top*, we see that the symmetry holds for the metastable transient up to the collapse time (vertical dotted line), thus the averaging in (11) is performed for time points in the metastable state suitably before. On the bottom panel, we show that, even without a metastable lattice, hexagonally packed lattices also display such a symmetry. In (b), U vs. $|\mathbf{P}|$ is shown for the metastable lattices ($N = 3, 4, 5, 6$, and 7), showing a good agreement with (12).

be applicable up to the collapse time. This is displayed in Fig. (12a) (*top row*). A straightforward consequence of this is the applicability of relation Eq. (12) in this regime. This is displayed in Fig. (12b), where the average in (11) is performed for time points before the collapse time. Data points here correspond to $N = 3, 4, 5, 6, 7$ simulations. Beyond this regime, relation (12) is indeed no longer applicable. We note that for hexagonally packed crystals, $|\mathbf{P}| \sim 10^{-1}$ in this scaling regime, thus we do not display the data points in Fig. (12b), though agreement with (11) also holds.

Appendix D: Derivation of dimensionality reduction for monodisperse dimers

To reduce the dimensionality of the dimer chain, using (B4), we have that

$$\frac{dR_x}{dt} = v_s (\cos(\theta_1) + \cos(\theta_2)) \quad (\text{D1})$$

$$\frac{dR_y}{dt} = v_s (\sin(\theta_1) + \sin(\theta_2)) = 0 \quad (\text{D2})$$

$$\frac{d\theta_1}{dt} = \chi_r (e_{x_1} \mathcal{I}_b - e_{y_1} \mathcal{I}_{11}^{(R_x)}) \quad (\text{D3})$$

$$\frac{d\theta_2}{dt} = \chi_r (e_{x_2} \mathcal{I}_b - e_{y_2} \mathcal{I}_{11}^{(R_x)}) = (e_{x_2} \mathcal{I}_b - e_{y_2} \mathcal{I}_{11}^{(R_x)}) \quad (\text{D4})$$

where we have defined

$$\mathcal{I}_b = \int_0^{t-1} \frac{2b}{(4D_c(t-t'))^2} \exp\left(\frac{-4b^2}{\mathcal{D}(t,t')}\right) dt' \quad (\text{D5})$$

$$\mathcal{I}_{11}^{(R_x)} = \frac{1}{2} \int_0^{t-1} \frac{\Delta R_x(t,t')}{(4D_c(t-t'))^2} \exp\left(\frac{-\Delta R_x^2}{\mathcal{D}(t,t')}\right) dt' = \mathcal{I}_{22}^{(x)}$$

where in the latter, we have used $x_1 = \frac{1}{2}R_x$ by the symmetry, and $\Delta x_{11}(t,t') = \Delta x_{22}(t,t')$. Thus, we see that the equations span a 3 dimensional phase space in $\{R_x, \theta_1, \theta_2\}$. To evaluate the integrals (D6), we use the fact that $\frac{b}{l_d} \ll 1$, which applies in Phase IV, to expand the integrand $\exp\left[-\frac{(R_x(t)-R_x(t'))^2}{4D_c(t-t')}\right] \approx 1 - O\left(\frac{b}{l_d}\right)^2$. Thus

$$\mathcal{I}_b = \int_0^{t-1} dt' \frac{2b}{(4D_c(t-t'))^2} \left[1 + O\left(\frac{b}{l_d}\right)^2\right] \approx \frac{b}{16D_c^2} \quad (\text{D6})$$

Having obtained the above, we now have:

$$\begin{aligned} \mathcal{I}_{11} &\approx \frac{1}{2} \dot{R}_x \int_0^{t-1} dt' \frac{1}{(4D_c)^2(t-t')} \left[1 + O\left(\frac{b}{l_d}\right)^2\right] \\ &\approx \frac{\dot{R}_x}{32D_c^2} \int_0^{t-1} \frac{1}{(t-t')} = \frac{\dot{R}_x}{32D_c^2} \ln(t). \end{aligned} \quad (\text{D7})$$

Thus, we have an explicit t dependence on the dynamics of (D6), a signature of history build-up of the chemicals due to (5).

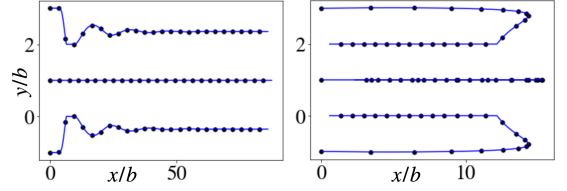


FIG. 13. Symmetric trails of ABA(-), BAB(-).

Appendix E: Symmetric trimers - ABA, BAB

For the ABA and BAB configurations, to solve for ϕ , we note that the cosine rule implies

$$(\Delta y_{13})^2 = 8b^2 (1 - \cos(\phi)) \quad (\text{E1})$$

the symmetry of the trimer problem means that the spring forces $F_{12} = -F_{21}$, $F_{23} = -F_{32}$, and $|F_{12}| = |F_{32}|$. We thus have the condition:

$$\frac{d(\Delta y_{13})}{dt} = 2v_s \sin(\theta_1) \quad (\text{E2})$$

Differentiating (E1), and applying (B12) we arrive at (22).

The symmetry of the trails (see Fig. (13)), further enables us to reduce the effective dimensionality. Using Eq. D, we consider the θ_1 equations for the ABA system:

$$\frac{d\theta}{dt} = \chi_r (\cos(\theta_1) J_{y_1} - \sin(\theta_1) J_{x_1}) \quad (\text{E3})$$

with

$$J_{y_1} = \int dt' \left[-\frac{\Delta y_{12}(t,t')}{\mathcal{D}^2(t,t')} \mathcal{F}_{12}^{(y)} + \frac{\Delta y_{13}(t,t')}{\mathcal{D}^2(t,t')} \mathcal{F}_{13}^{(y)} \right] \quad (\text{E4})$$

where we have inserted entries from (20). We can show that $J_{y_1} = -J_{y_3}$ by noting the following relations (analogous to (B12))

$$\Delta y_{12} = -\Delta y_{32}, \quad \Delta y_{13} = -\Delta y_{31} \quad (\text{E5})$$

along with $J_{x_1} = J_{x_3}$ implies that

$$\frac{d\theta_1}{dt} = -\frac{d\theta_3}{dt} \quad (\text{E6})$$

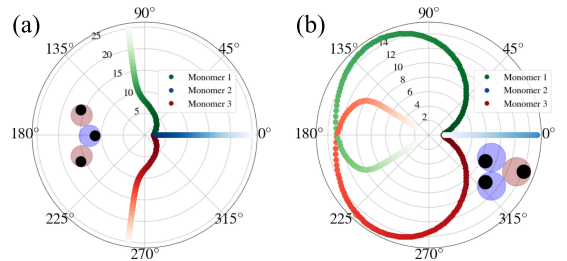


FIG. 14. Plots analogous to Figure 7 are displayed, this time for ABA(+), BAB(+) configurations.

as is also evident in Fig. (7) and SI Video 8 [33]. Thus, at the fixed point orientations θ_i^* , we have a stably propelling trimer governed by

$$\frac{dR_x}{dt} = v_s \left(2 \cos(\theta_1) + \cos(\theta_2) \right) \quad (\text{E7})$$

thus giving (23) and (24)

Appendix F: Trimers with AB(+): Results

The results for ABA(+), BAB(+) trimers, are displayed here in Fig. (14). ABA(+) reproduces a chemo-repulsive trimer, BAB(+) reproduces a chemo-attractive trimer. Compare this with results of Fig.(7).

-
- [1] M. E. Cates and J. Tailleur, Motility-induced phase separation, *Annu. Rev. Condens. Matter Phys.* **6**, 219 (2015).
- [2] C. Bechinger, R. Di Leonardo, H. Löwen, C. Reichhardt, G. Volpe, and G. Volpe, Active particles in complex and crowded environments, *Rev. Mod. Phys.* **88**, 045006 (2016).
- [3] R. E. Goldstein, Green algae as model organisms for biological fluid dynamics, *Ann. Rev. Fluid Mech.* **47**, 343 (2015).
- [4] S. J. Ebbens and J. R. Howse, In pursuit of propulsion at the nanoscale, *Soft Matter* **6**, 726 (2010).
- [5] J. L. Anderson, Colloid transport by interfacial forces, *Annu. Rev. Fluid Mech.* **21**, 61 (1989).
- [6] A. Snezhko and I. S. Aranson, Magnetic manipulation of self-assembled colloidal asters, *Nat. Mater.* **10**, 698 (2011).
- [7] B. Biswas, D. Mitra, F. Kp, S. Bhat, A. Chatterji, and G. Kumaraswamy, Rigidity dictates spontaneous helix formation of thermoresponsive colloidal chains in poor solvent, *ACS Nano* **15**, 19702 (2021).
- [8] H. R. Vutukuri, B. Bet, R. Van Roij, M. Dijkstra, and W. T. Huck, Rational design and dynamics of self-propelled colloidal bead chains: from rotators to flagella, *Sci. Rep.* **7**, 16758 (2017).
- [9] J. Zhang and S. Granick, Natural selection in the colloid world: active chiral spirals, *Farad. Disc.* **191**, 35 (2016).
- [10] D. Nishiguchi, J. Iwasawa, H.-R. Jiang, and M. Sano, Flagellar dynamics of chains of active janus particles fueled by an AC electric field, *New J. Phys.* **20**, 015002 (2018).
- [11] T. Yang, B. Sprinkle, Y. Guo, J. Qian, D. Hua, A. Donev, D. W. Marr, and N. Wu, Reconfigurable microbots folded from simple colloidal chains, *Proc. Natl. Acad. Sci.* **117**, 18186 (2020).
- [12] R. Reyes Garza, N. Kyriakopoulos, Z. M. Cenev, C. Rigoni, and J. V. Timonen, Magnetic quincke rollers with tunable single-particle dynamics and collective states, *Sci. Adv.* **9**, eadh2522 (2023).
- [13] J. Yan, M. Bloom, S. C. Bae, E. Luijten, and S. Granick, Linking synchronization to self-assembly using magnetic janus colloids, *Nature* **491**, 578 (2012).
- [14] Z. Zeravcic, V. N. Manoharan, and M. P. Brenner, Size limits of self-assembled colloidal structures made using specific interactions, *Proc. Natl. Acad. Sci.* **111**, 15918 (2014).
- [15] Z. Zeravcic, V. N. Manoharan, and M. P. Brenner, Colloquium: Toward living matter with colloidal particles, *Rev. Mod. Phys.* **89**, 031001 (2017).
- [16] R. Soto and R. Golestanian, Self-assembly of active colloidal molecules with dynamic function, *Phys. Rev. E* **91**, 052304 (2015).
- [17] K. J. Bishop, S. L. Biswal, and B. Bharti, Active colloids as models, materials, and machines, *Annu. Rev. Chem. Biomol.* **14**, 1 (2023).
- [18] A. Sengupta, S. van Teeffelen, and H. Löwen, Dynamics of a microorganism moving by chemotaxis in its own secretion, *Phys. Rev. E* **80**, 031122 (2009).
- [19] J. Taktikos, V. Zaburdaev, and H. Stark, Collective dynamics of model microorganisms with chemotactic signaling, *Phys. Rev. E* **85**, 051901 (2012).
- [20] B. V. Hokmabad, J. Agudo-Canalejo, S. Saha, R. Golestanian, and C. C. Maass, Chemotactic self-caging in active emulsions, *Proc. Natl. Acad. Sci.* **119**, e2122269119 (2022).
- [21] N. Mittal, E. O. Budrene, M. P. Brenner, and A. Van Oudenaarden, Motility of escherichia coli cells in clusters formed by chemotactic aggregation, *Proc. Natl. Acad. Sci.* **100**, 13259 (2003).
- [22] D. E. Jackson, S. J. Martin, M. Holcombe, and F. L. Ratnieks, Longevity and detection of persistent foraging trails in pharaoh's ants, *monomorium pharaonis* (L.), *Animal Behaviour* **71**, 351 (2006).
- [23] A. Gelimson, K. Zhao, C. K. Lee, W. T. Kranz, G. C. Wong, and R. Golestanian, Multicellular self-organization of *P. aeruginosa* due to interactions with secreted trails, *Phys. Rev. Lett.* **117**, 178102 (2016).
- [24] K. Zhao, B. S. Tseng, B. Beckerman, F. Jin, M. L. Gibiansky, J. J. Harrison, E. Luijten, M. R. Parsek, and G. C. Wong, Psl trails guide exploration and microcolony formation in pseudomonas aeruginosa biofilms, *Nature* **497**, 388 (2013).
- [25] W. T. Kranz, A. Gelimson, K. Zhao, G. C. Wong, and R. Golestanian, Effective dynamics of microorganisms that interact with their own trail, *Phys. Rev. Lett.* **117**, 038101 (2016).
- [26] W. T. Kranz and R. Golestanian, Trail-mediated self-interaction, *The Journal of Chemical Physics* **150** (2019).
- [27] M. Kumar, A. Murali, A. G. Subramaniam, R. Singh, and S. Thutupalli, Emergent dynamics due to chemohydrodynamic self-interactions in active polymers, arXiv preprint arXiv:2303.10742 (2023).
- [28] S. Herminghaus, C. C. Maass, C. Krüger, S. Thutupalli, L. Goehring, and C. Bahr, Interfacial mechanisms in active emulsions, *Soft matter* **10**, 7008 (2014).
- [29] There are additional time scales $\tau_d = \frac{D_c}{v_s^2}$ and $\tau_t = \frac{b^2}{\chi_t}$. We ignore these in the analysis.
- [30] With the definitions given in equations (6) and (7) there are additional valid (10 in total) Peclet numbers. However, these additional feasible dimensionless parameters in our system e.g. one could define $\mathcal{A} = \frac{v_s b^2}{\chi_r} = \frac{\tau}{\tau_f}$, are

- not systematically studied here (indeed they do not affect our bigger picture findings).
- [31] W. Helfrich, Elastic properties of lipid bilayers: theory and possible experiments, *Z. Naturforsch* **28**, 693 (1973).
- [32] M. Doi and S. F. Edwards, *The theory of polymer dynamics*, Vol. 73 (Oxford University Press, 1988).
- [33] See the supplemental material at this url: <https://gitlab.com/softmatter/ags/-/wikis/P2>
- [34] Y. Tsori and P.-G. De Gennes, Self-trapping of a single bacterium in its own chemoattractant, *EPL* **66**, 599 (2004).
- [35] R. Soto and R. Golestanian, Self-assembly of catalytically active colloidal molecules: Tailoring activity through surface chemistry, *Phys. Rev. Lett.* **112**, 068301 (2014).
- [36] J. Agudo-Canalejo and R. Golestanian, Active phase separation in mixtures of chemically interacting particles, *Phys. Rev. Lett.* **123**, 018101 (2019).
- [37] S. Saha, R. Golestanian, and S. Ramaswamy, Clusters, asters, and collective oscillations in chemotactic colloids, *Phys. Rev. E* **89**, 062316 (2014).
- [38] J. Palacci, S. Sacanna, A. P. Steinberg, D. J. Pine, and P. M. Chaikin, Living crystals of light-activated colloidal surfers, *Science* **339**, 936 (2013).
- [39] R. Singh and R. Adhikari, Universal hydrodynamic mechanisms for crystallization in active colloidal suspensions, *Phys. Rev. Lett.* **117**, 228002 (2016).
- [40] S. Thutupalli, D. Geyer, R. Singh, R. Adhikari, and H. A. Stone, Flow-induced phase separation of active particles is controlled by boundary conditions, *Proc. Natl. Acad. Sci.* **115**, 5403 (2018).
- [41] I. Theurkauff, C. Cottin-Bizonne, J. Palacci, C. Ybert, and L. Bocquet, Dynamic clustering in active colloidal suspensions with chemical signaling, *Phys. Rev. Lett.* **108**, 268303 (2012).
- [42] R. Niu, A. Fischer, T. Palberg, and T. Speck, Dynamics of binary active clusters driven by ion-exchange particles, *ACS Nano* **12**, 10932 (2018).
- [43] T. Yu, P. Chuphal, S. Thakur, S. Y. Reigh, D. P. Singh, and P. Fischer, Chemical micromotors self-assemble and self-propel by spontaneous symmetry breaking, *Chem. Commun.* **54**, 11933 (2018).
- [44] F. Schmidt, B. Liebchen, H. Löwen, and G. Volpe, Light-controlled assembly of active colloidal molecules, *J. Chem. Phys.* **150** (2019).
- [45] J. Grauer, H. Löwen, A. Be'er, and B. Liebchen, Swarm hunting and cluster ejections in chemically communicating active mixtures, *Sci. Rep.* **10**, 5594 (2020).
- [46] C. H. Meredith, P. G. Moerman, J. Groenewold, Y.-J. Chiu, W. K. Kegel, A. van Blaaderen, and L. D. Zarzar, Predator-prey interactions between droplets driven by non-reciprocal oil exchange, *Nat. Chem.* **12**, 1136 (2020).
- [47] S. Saha, J. Agudo-Canalejo, and R. Golestanian, Scalar active mixtures: The nonreciprocal Cahn-Hilliard model, *Phys. Rev. X* **10**, 041009 (2020).
- [48] Z. You, A. Baskaran, and M. C. Marchetti, Nonreciprocity as a generic route to traveling states, *Proc. Natl. Acad. Sci.* **117**, 19767 (2020).
- [49] C. Scheibner, A. Souslov, D. Banerjee, P. Surówka, W. T. Irvine, and V. Vitelli, Odd elasticity, *Nat. Phys.* **16**, 475 (2020).
- [50] L. Braverman, C. Scheibner, B. VanSaders, and V. Vitelli, Topological defects in solids with odd elasticity, *Phys. Rev. Lett.* **127**, 268001 (2021).
- [51] T. H. Tan, A. Mietke, J. Li, Y. Chen, H. Higinbotham, P. J. Foster, S. Gokhale, J. Dunkel, and N. Fakhri, Odd dynamics of living chiral crystals, *Nature* **607**, 287 (2022).
- [52] M. Tsyganov, J. Brindley, A. Holden, and V. Biktaşhev, Quasisoliton interaction of pursuit-evasion waves in a predator-prey system, *Phys. Rev. Lett.* **91**, 218102 (2003).
- [53] A. Sengupta, T. Kruppa, and H. Löwen, Chemotactic predator-prey dynamics, *Phys. Rev. E* **83**, 031914 (2011).
- [54] R. Dreyfus, J. Baudry, M. L. Roper, M. Fermigier, H. A. Stone, and J. Bibette, Microscopic artificial swimmers, *Nature* **437**, 862 (2005).
- [55] K. Ishimoto, C. Moreau, and K. Yasuda, Self-organized swimming with odd elasticity, *Phys. Rev. E* **105**, 064603 (2022).
- [56] K. Ishimoto, C. Moreau, and K. Yasuda, Odd elastohydrodynamics: non-reciprocal living material in a viscous fluid, arXiv preprint arXiv:2306.07162 (2023).
- [57] C. Fang-Yen, M. Wyart, J. Xie, R. Kawai, T. Kodger, S. Chen, Q. Wen, and A. D. Samuel, Biomechanical analysis of gait adaptation in the nematode *Caenorhabditis Elegans*, *Proc. Natl. Acad. Sci.* **107**, 20323 (2010).
- [58] F. J. Segerer, F. Thüroff, A. P. Alberola, E. Frey, and J. O. Rädler, Emergence and persistence of collective cell migration on small circular micropatterns, *Phys. Rev. Lett.* **114**, 228102 (2015).
- [59] A. S. Chin, K. E. Worley, P. Ray, G. Kaur, J. Fan, and L. Q. Wan, Epithelial cell chirality revealed by three-dimensional spontaneous rotation, *Proc. Natl. Acad. Sci.* **115**, 12188 (2018).
- [60] A. Kumar, A. Maitra, M. Sumit, S. Ramaswamy, and G. Shivashankar, Actomyosin contractility rotates the cell nucleus, *Sci. Rep.* **4**, 3781 (2014).